Molecular Cell

Article

Threonine-rich carboxyl-terminal extension drives aggregation of stalled polypeptides

Graphical abstract

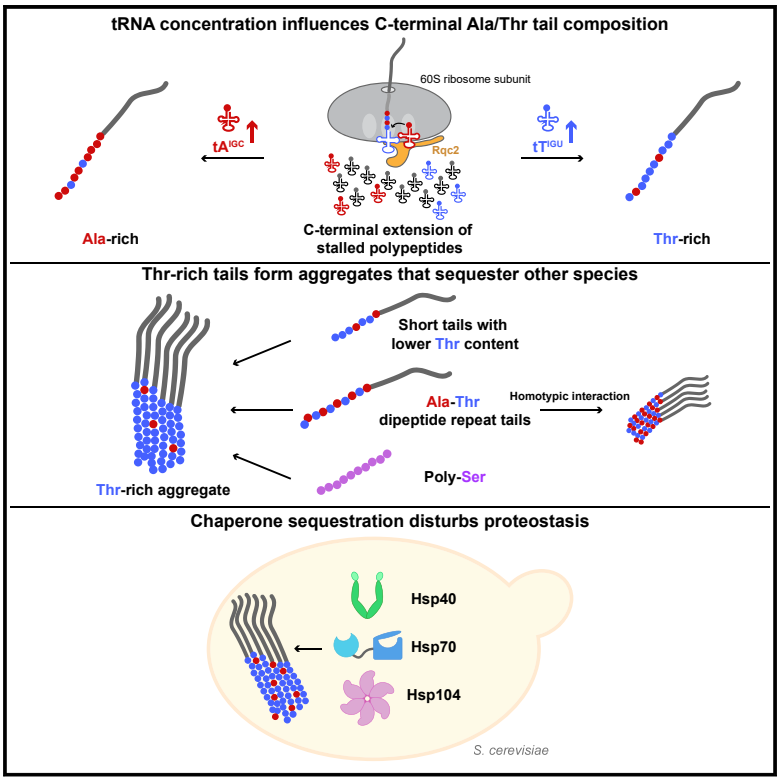

Highlights

- tRNA levels influence the composition of C-terminal extensions of stalled polypeptides
- Threonine-rich extensions form detergent-insoluble aggregates
- Threonine-based protein aggregates display robust seeding effects
- Polythreonine aggregates sequester polyserine

Authors

Weili Denyse Chang, Mi-Jeong Yoon, Kian Hua Yeo, Young-Jun Choe

Correspondence

yjchoe@ntu.edu.sg

In brief

When ribosomes stall during translation of defective mRNAs, the resulting incomplete polypeptides form detergent-insoluble aggregates. Chang & Yoon et al. demonstrate that threonine residues drive this aberrant protein aggregation in *Saccharomyces cerevisiae*. This study uncovers a distinctive protein aggregation mechanism.

Chang et al., 2024, Molecular Cell *84*, 4334–4349
November 21, 2024
https://doi.org/10.1016/j.molcel.2024.10.011

CellPress

CellPress
OPEN ACCESS

Molecular Cell

Article

Threonine-rich carboxyl-terminal extension drives aggregation of stalled polypeptides

Weili Denyse Chang,[1,2] Mi-Jeong Yoon,[1,2] Kian Hua Yeo,[1] and Young-Jun Choe[1,3,*]
[1]School of Biological Sciences, Nanyang Technological University, Singapore 637551, Singapore
[2]These authors contributed equally
[3]Lead contact
*Correspondence: yjchoe@ntu.edu.sg
https://doi.org/10.1016/j.molcel.2024.10.011

SUMMARY

Ribosomes translating damaged mRNAs may stall and prematurely split into their large and small subunits. The split large ribosome subunits can continue elongating stalled polypeptides. In yeast, this mRNA-independent translation appends the C-terminal alanine/threonine tail (CAT tail) to stalled polypeptides. If not degraded by the ribosome-associated quality control (RQC), CAT-tailed stalled polypeptides form aggregates. How the CAT tail, a low-complexity region composed of alanine and threonine, drives protein aggregation remains unknown. In this study, we demonstrate that C-terminal polythreonine or threonine-enriched tails form detergent-resistant aggregates. These aggregates exhibit a robust seeding effect on shorter tails with lower threonine content, elucidating how heterogeneous CAT tails co-aggregate. Polythreonine aggregates sequester molecular chaperones, disturbing proteostasis and provoking the heat shock response. Furthermore, polythreonine cross-seeds detergent-resistant polyserine aggregation, indicating structural similarity between the two aggregates. This study identifies polythreonine and polyserine as a distinct group of aggregation-prone protein motifs.

INTRODUCTION

Defective mRNAs, resulting from erroneous processing or exposure to environmental stressors such as reactive oxygen species, UV radiation, and alkylating chemicals, can cause ribosomes to stall at the site of lesions.[1–4] This poses two challenges to cells: loss of active ribosomes and emergence of potentially toxic incomplete stalled polypeptides. To resolve these problems, eukaryotic cells have evolved a mechanism to rescue stalled ribosomes by splitting them into the large and small subunits.[5,6] Notably, the rescued large ribosome subunits are subject to the ribosome-associated quality control (RQC) pathway to clear stalled polypeptides, thereby overcoming both challenges associated with ribosome stalling.[7–9]

Since mRNAs can be translated by multiple ribosomes simultaneously, stalled ribosomes would collide with trailing ribosomes, forming disomes.[10,11] These disomes undergo ubiquitin modification,[12–15] which triggers a splitting reaction.[16–20] The resultant large ribosomal subunit (LSU) with an anchored peptidyl-tRNA is recognized by Rqc2 (in yeast and NEMF in mammals).[21,22] Rqc2 subsequently recruits the RQC E3 ligase Ltn1,[21–23] positioning its RING domain near the ribosomal exit tunnel, which facilitates the efficient ubiquitylation of the LSU-anchored stalled polypeptides. However, because Ltn1 is tethered to the LSU, it cannot actively survey lysine residues in stalled polypeptides. Consequently, Ltn1 could fail to recognize certain substrates that lack readily accessible lysine residues near the exit tunnel. To overcome this limitation, Rqc2 extends the carboxyl-termini (C-termini) of LSU-anchored stalled polypeptides by incorporating alanine and threonine residues.[22,24–26] Extension of the C-terminal alanine/threonine tail (CAT tail) pushes the C-terminal segments of stalled polypeptides outside the ribosomal exit tunnel, rendering previously hidden lysine residues available for polyubiquitylation.[27]

Rqc2 extends CAT tails by recruiting specific alanyl- and threonyl-tRNAs to the A site of the LSU independently of mRNA and the small ribosomal subunit.[22] If CAT-tailed polypeptides are released from the LSU without prior ubiquitylation by Ltn1, CAT tails themselves could act as a degradation signal that can be recognized by other cytosolic E3 ligases.[28,29] Therefore, CAT tails facilitate the degradation of stalled polypeptides both on and off the ribosome.

If not cleared by RQC and downstream cytosolic degradation pathways, the yeast CAT tail drives the aggregation of stalled polypeptides.[30–32] These detergent-resistant aggregates sequester diverse chaperones and thereby disturb general protein quality control pathways, provoking the heat shock response (HSR). Indeed, RQC components were initially identified as genetic modifiers of the HSR; deletion of *LTN1* elevated the HSR even under normal conditions.[33] Interestingly, the HSR in *ltn1*Δ cells was found to be dependent on Rqc2 and its CAT tailing activity,[22,33] suggesting that the aggregation of endogenous stalled

polypeptides induced by CAT tails could stress cells. Notably, a recent study showed that ribosomal stalling increases with aging in model organisms, including *S. cerevisiae* and *C. elegans*.[34] Increased ribosomal stalling could overwhelm the RQC capacity, leading to excessive stalled polypeptides, which form aggregates and disturb proteostasis during aging. In yeast, CAT tails promote the age-dependent aggregation of stalled polypeptides.

However, the mechanism by which CAT tails, low-complexity regions composed solely of alanine and threonine, drive protein aggregation remains unknown. In this study, we demonstrate that CAT tails undergo threonine-based aggregation. Threonine-rich protein extensions can aggregate when they exceed a certain length threshold. Once formed, these aggregates recruit shorter extensions with relatively lower threonine content that are unable to initiate aggregation independently. Consequently, threonine residues mediate the co-aggregation of heterogeneous CAT tails. Similar to endogenous CAT tail aggregates, polythreonine aggregates effectively sequester multiple molecular chaperones, thereby disturbing proteostasis. Additionally, we discover an interaction between polythreonine and polyserine, both of which share similar side chains, providing insight into the structural basis of their detergent-resistant aggregation.

RESULTS

tRNA$^{Thr(IGU)}$ enhances aggregation of stalled polypeptides

We employed GFP reporter mRNAs to induce ribosome stalling. The reporters either contained CGA codon repeats or lacked a stop codon (non-stop), allowing translation into the polyadenosine tail.[1,35] Both CGA codon repeats and polyadenosine tracts adopt decoding-incompatible conformations within translating ribosomes.[36,37] In wild-type (WT) cells, stalled GFP was minimally detectable due to RQC degradation (Figures 1A and S1A, lanes 1). By contrast, stalled GFP remained undegraded in *ltn1*Δ cells and formed detergent-insoluble aggregates due to the CAT tail extension. These aggregates were detected by semi-denaturing detergent agarose gel electrophoresis (SDD-AGE)[38] (Figures 1A and S1A, lanes 2). *RQC2* deletion abrogated CAT tail extension, thereby preventing aggregation of stalled GFP (Figures 1A and S1A, lanes 3). To investigate the mechanism driving CAT tail aggregation, we modulated the levels of alanyl- and threonyl-tRNAs. CAT tail synthesis is not directed by mRNAs but is determined by the interaction between Rqc2 and substrate tRNAs[22] (Figure 1B). The yeast tRNA pool encompasses two alanine and three threonine isoacceptors (http://gtrnadb.ucsc.edu/). We individually overexpressed each alanine or threonine tRNA (Figure 1C) to assess their impact on CAT-tailed polypeptide aggregation. Remarkably, SDD-AGE revealed heightened aggregation of stalled GFP reporters when tRNA$^{Thr(IGU)}$ was overexpressed, while the other tRNAs showed no such effect (Figures 1D and S1B). However, tRNA$^{Thr(IGU)}$ overexpression alone did not induce aggregation of stalled GFP when Rqc2 was absent (Figures 1E and S1C), indicating that the observed effect of tRNA$^{Thr(IGU)}$ was mediated through CAT tails. Consistently, tRNA$^{Thr(IGU)}$ has been previously identified as an Rqc2 substrate.[22] Overexpression of tRNA$^{Thr(IGU)}$ might have increased the length of CAT tails; however, this potential increase was not detectable by gel electrophoresis (Figure S1D). Importantly, tRNA$^{Thr(IGU)}$ overexpression indeed resulted in a slight increase in the threonine content of CAT tails (Figure S1E). Interestingly, the alanine content conversely decreased, indicating competition between alanine and threonine for incorporation into CAT tails.

CAT-tailed proteins in *ltn1*Δ cells are known to induce the HSR.[22,33,39] To further investigate the effect of alanyl- or threonyl-tRNA overexpression on CAT tails, we monitored the HSR using a GFP reporter under a stress-inducible promoter (Figure S1F). While overexpressed tRNAs tended to slightly induce the HSR, tRNA$^{Thr(IGU)}$, which increased stalled polypeptide aggregation, prominently enhanced the HSR in *ltn1*Δ cells (Figure 1F). It was intriguing that overexpression of a single tRNA could significantly enhance the HSR in the absence of other proteotoxic stressors. However, the same tRNA induced only modest HSR in cells where CAT-tailed proteins would not exist (Figure 1G); endogenous stalled polypeptides would be degraded in WT cells, and CAT tail synthesis is absent in *ltn1*Δ*rqc2*Δ cells. Taken together, the increased threonine content in CAT tails enhances the aggregation of stalled polypeptides, thereby impacting cellular proteostasis, as evidenced by the increase in the HSR.

tRNA$^{Ala(IGC)}$ reduces proteotoxicity of stalled polypeptides

Given that the yeast CAT tail comprises only alanine and threonine, alanyl-tRNAs were expected to display a contrasting effect to tRNA$^{Thr(IGU)}$. However, no alanyl-tRNAs visibly decreased the aggregation of stalled GFP reporters (Figures 1D and S1B). Therefore, we conducted additional assays to thoroughly examine the effects of alanyl-tRNA overexpression. A previous study found that overproduced Rqc2 elevates the HSR in *ltn1*Δ cells[39] (Figure S1G), likely due to increased CAT tailing and subsequent aggregation of endogenous stalled polypeptides. Indeed, *RQC2* overexpression in *ltn1*Δ cells heightened detergent-resistant aggregation of Sis1 (Figure S1H), a chaperone that associates with CAT-tailed polypeptides.[30–32] The emergence of a Sis1 smear indicated enhanced aggregation of endogenous stalled polypeptides, as no other recombinant stalling reporters were used in the experiment. By contrast, a mutant Rqc2 defective in CAT tailing activity[22] neither induced the HSR nor augmented Sis1 aggregation in *ltn1*Δ cells (Figures S1G and S1H), further confirming that the observed effects of Rqc2 overproduction were via CAT tailing. In WT cells, where the intact RQC system would degrade endogenous stalled polypeptides, *RQC2* overexpression did not induce the HSR or Sis1 aggregation (Figures S1G and S1H).

We next examined the effects of alanyl- and threonyl-tRNAs on the HSR induced by *RQC2* overexpression (Figure 1H). Threonyl-tRNAs, including tRNA$^{Thr(IGU)}$, slightly increased the HSR further. However, the effect was limited, suggesting that the HSR had nearly reached its maximum. Surprisingly, tRNA$^{Ala(IGC)}$ significantly dampened the HSR, indicating that the tRNA reduced CAT tail-associated proteotoxicity. Accordingly, we examined whether tRNA$^{Ala(IGC)}$ could rescue the growth of cells stressed by CAT-tailed proteins. The combined

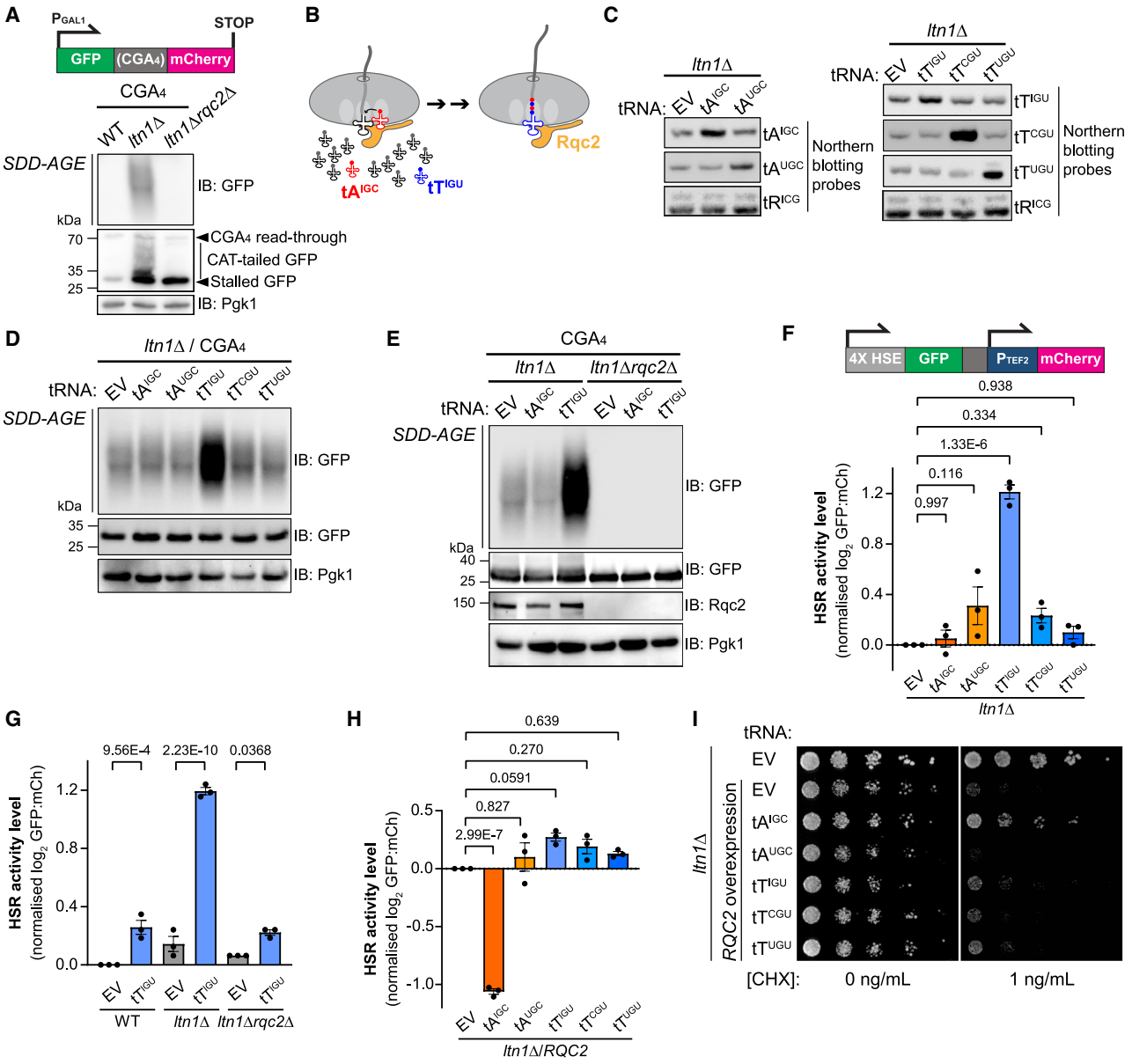

Figure 1. Effects of overexpressed tRNA$^{Thr(IGU)}$ and tRNA$^{Ala(IGC)}$ on CAT tail aggregation

(A) A stalling reporter with four internal repeats of the CGA codon (CGA_4) was expressed under the *GAL1* promoter. Cell lysates separated using SDD-AGE and SDS-PAGE were analyzed by anti-GFP immunoblotting (IB). Although some ribosomes translated through the CGA codon repeats (arrowhead: CGA_4 read-through), most ribosomes stalled during translation (arrowhead: stalled GFP). Pgk1 served as a loading control.

(B) Schematic of CAT tail synthesis. tRNA$^{Ala(IGC)}$ (tA^{IGC}) and tRNA$^{Thr(IGU)}$ (tT^{IGU}) have been previously identified as Rqc2 substrates.[22]

(C) High-copy vectors carrying tRNA^{Ala} (tA) and tRNA^{Thr} (tT) genes were individually introduced into *ltn1*Δ cells. Northern blotting was performed using probes specific to each tRNA. tRNA$^{Arg(ICG)}$ (tR^{ICG}) served as a loading control. EV, empty vector.

(D and E) The CGA_4 reporter (A) was expressed in *ltn1*Δ or *ltn1*Δ*rqc2*Δ cells, overexpressing each indicated alanine or threonine tRNA.

(F–H) The indicated tRNAs were overexpressed in WT or RQC-defective cells containing a chromosomally integrated HSR reporter.[33] GFP, expressed under a promoter with four repeats of the heat shock element (HSE), was normalized to mCherry, expressed under the constitutive *TEF2* promoter. GFP and mCherry expression levels were analyzed using flow cytometry. Cells were cultured at 25°C in glucose media (F and G) or galactose media to induce *RQC2* expression under the *GAL1* promoter (H). EV, empty vector; black dot, individual data point; error bar, SEM ($n = 3$). p values were obtained by one-way ANOVA followed by Tukey's range test.

(I) *RQC2* and tRNA overexpression vectors were co-transformed into *ltn1*Δ cells as indicated. Empty vectors served as controls. *RQC2* expression from the vector was driven by the *GAL1* promoter. Cells were serially diluted fivefold and spotted on galactose plates selective for vectors, with the absence or presence of 1 ng/mL cycloheximide (CHX).

overexpression of *RQC2* and alanyl- or threonyl-tRNAs had minimal impact on cell growth (Figure 1I, left plate). To introduce ribosome stalling stress, we used cycloheximide at a concentration typically non-toxic to yeast cells (Figure 1I, right plate, first row). This minute translation stress caused severe toxicity when Rqc2 was overproduced[39] (Figure 1I, right plate, second row). Remarkably, $tRNA^{Ala(IGC)}$ co-expression partially rescued this growth defect (Figure 1I, right plate, third row). Overall, $tRNA^{Ala(IGC)}$ mitigated the proteotoxic effects of stalled polypeptides, indicating reduced CAT tail aggregation. Thus, we reevaluated the effects of alanyl-tRNA overexpression on GFP stalling reporter aggregation and found that its aggregation was detectably reduced when the level of $tRNA^{Ala(IGC)}$ was increased beyond that of the previous experiment in Figure 1D (Figures S1I and S1J). Notably, $tRNA^{Ala(IGC)}$ overexpression increased the alanine content in CAT tails while reducing the threonine content (Figure S1K). Taken together, only $tRNA^{Ala(IGC)}$ and $tRNA^{Thr(IGU)}$ among the five alanine and threonine isoacceptors modulated CAT tail aggregation, confirming a previous study that identified the two tRNAs as Rqc2 substrates.[22]

Polythreonine forms detergent-insoluble aggregates

The opposing effects of the two Rqc2 substrates, $tRNA^{Ala(IGC)}$ and $tRNA^{Thr(IGU)}$, prompted an investigation into the behavior of polyalanine and polythreonine tails. We constructed GFP reporters with C-terminal polyalanine or polythreonine tails of varying lengths (10, 20, or 30 residues). The reporters, which do not induce ribosome stalling, were expressed in WT cells. Intriguingly, 30-amino acid-long polythreonine (hereafter, T30) displayed a high-molecular-weight (HMW) smear during gel electrophoresis (Figure 2A). Additionally, microscopy revealed GFP-T30 inclusions (Figure 2B), indicating that the observed HMW smear represented detergent-insoluble aggregates. Fluorescence recovery after photobleaching (FRAP) analysis revealed that GFP-T30 was immobile within these inclusions (Figure 2C), further confirming solid-state aggregation. GFP-T30 puncta were cytosolic; polythreonine tails did not direct proteins to other subcellular organelles such as nuclei or vacuoles (Figure S2A). By contrast, GFPs with C-terminal alanine tails tended to localize in the nucleus but did not form inclusions (Figure S2B). To determine the minimal length required for polythreonine aggregation, tail lengths were gradually decreased from 30 to 20 residues. HMW smears were observed for T22 using SDD-AGE (Figure 2D), while microscopic inclusions were visible starting at T23 (Figure 2E). Thus, the minimum length for polythreonine aggregation consistently lay between T22 and T23, while aggregation substantially escalated between T25 and T30. The position of polythreonine stretches within proteins exerted little effect on their aggregation. For instance, a construct with T30 inserted between GFP and mCherry (GFP-T30-mCh) also formed detergent-resistant aggregates, despite T30 not being at the C terminus (Figure S2C). To ascertain polythreonine-autonomous aggregation, we expressed polythreonine in peptide forms fused to the FLAG tag. Remarkably, anti-FLAG immunofluorescence microscopy revealed inclusions of polythreonine peptides (Figure 2F). Interestingly, FLAG-T20 also formed inclusions, albeit less frequently than FLAG-T30, indicating that 20 threonine residues were sufficient to drive aggregation. For GFP-T20 (Figures 2D and 2E), steric hindrance between the globular GFP domains might have obstructed aggregate growth. FLAG-T10 peptide was undetectable (Figure 2F), likely due to decay by cytosolic peptidases.[40,41] Similarly, FLAG-T30 and FLAG-T20 peptides exhibited minimal cytosolic background, suggesting that soluble peptides were degraded, and only aggregated forms were retained in cells. Consistent with immunofluorescence microscopy, FLAG-T30 peptide displayed detergent-resistant HMW smears during gel electrophoresis (Figure 2G). However, HMW smears of FLAG-T20 were not detected, likely due to its lower aggregation propensity and/or lower stability of T20 aggregates. Peptide aggregation was similarly observed using a different epitope, the hemagglutinin (HA) tag. HA-T30 exhibited detergent-insoluble HMW smears (Figure S2D), which could be pelleted by centrifugation (Figure S2E). Thus, the polythreonine tail, not epitope tags, was the key driver of aggregation.

We next compared the aggregation propensity of polythreonine with those of polyglutamine and polyasparagine, both of which are well-studied aggregation-prone homopolymeric amino acids. However, neither polyglutamine nor polyasparagine exhibited microscopic inclusions or HMW gel smears at the length of 30 residues (Figures 2H and S2F), indicating that polythreonine is more prone to aggregation than polyglutamine and polyasparagine.

Aggregation of alanine-interrupted polythreonine

Although our data suggested polythreonine aggregation as a likely mechanism of CAT tail aggregation, two questions remained to be addressed: first, whether Rqc2 could synthesize CAT tails longer than the critical length of polythreonine aggregation, and second, whether aggregation strictly requires consecutive threonine residues or if alanine interruptions could be tolerated since endogenous CAT tails are more likely to be a mixture of alanine and threonine.

To address the first question on CAT tail length, we used a GFP reporter followed by CGA codon repeats, a potent inducer of ribosomal stalling. The CAT tail smear was readily discernible when comparing the *ltn1*Δ cell lysate to the *ltn1*Δ*rqc2*Δ cell lysate (Figure 3A, lanes 3 and 4). This smear was compared with GFP-T30, a hard-coded tail exceeding the critical length of aggregation (T22-23, Figures 2D and 2E). The addition of a C-terminal T30 tail noticeably altered GFP migration during gel electrophoresis (Figure 3A, lanes 1 and 2). Notably, the CAT tail smear extended beyond the GFP-T30 band (Figure 3A, lanes 2 and 3), indicating a fraction of natural CAT tails was longer than 30 residues, thereby potentially capable of aggregation.

To address the second question on the necessity of consecutive threonine residues for aggregation, we introduced varying numbers of alanine residues, from one to ten, into polythreonine stretches while maintaining the total length of 30 amino acids (Figure 3B). As the number of interrupting alanine residues increased, detergent-insoluble aggregation tended to decrease in SDD-AGE and polyacrylamide gel pockets (Figure 3B). This observation was consistent with the $tRNA^{Ala(IGC)}$-induced reduction in stalled polypeptide aggregation (Figure S1I). Overall, our data indicated a pro-aggregation effect of threonine residues and an anti-aggregation effect of alanine residues in CAT tails.

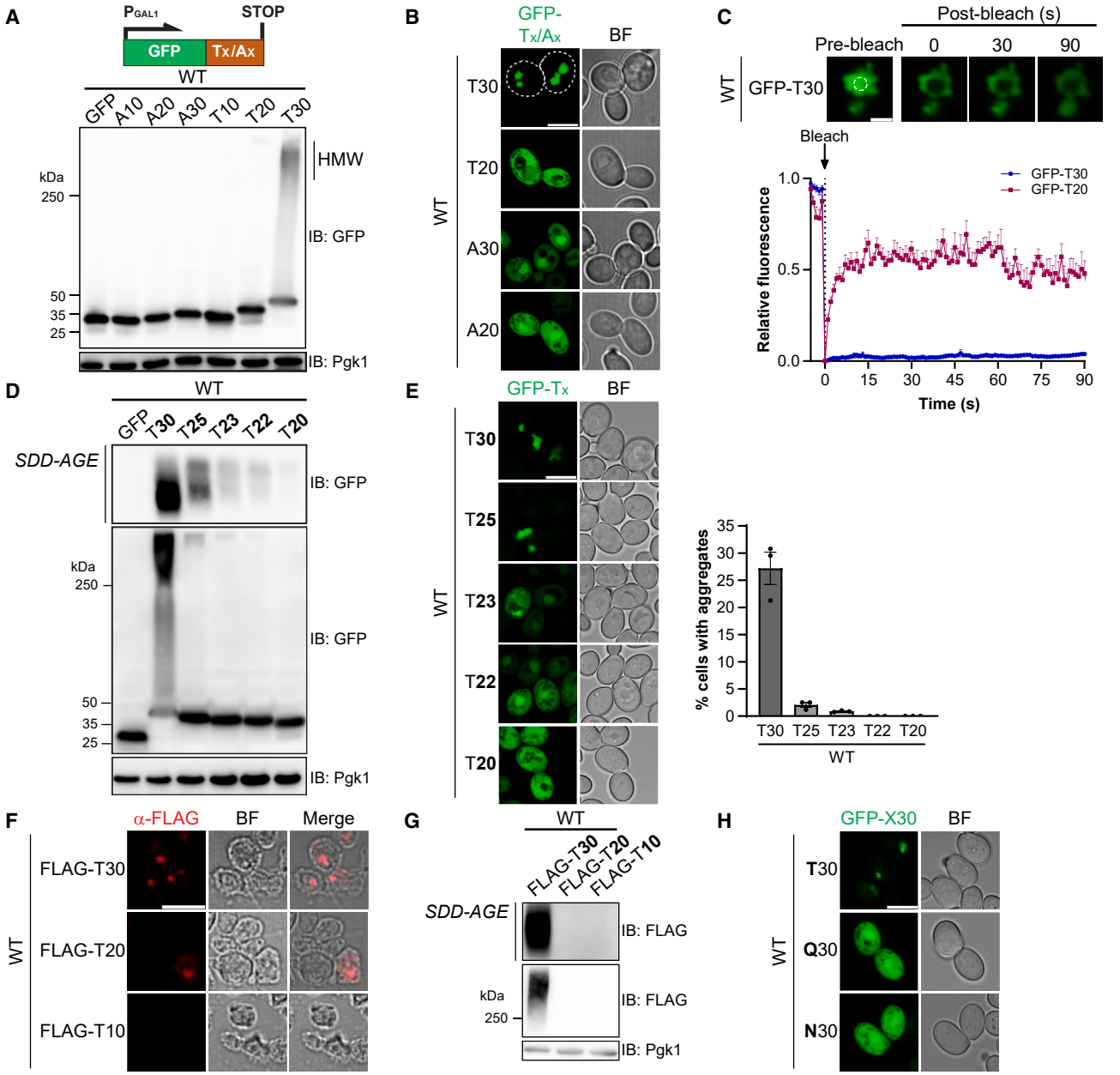

Figure 2. Polythreonine forms detergent-insoluble aggregates

(A) GFPs with a polyalanine or polythreonine tail were expressed under the *GAL1* promoter in WT cells. Cell lysates were analyzed by SDS-PAGE, followed by anti-GFP immunoblotting (IB). Pgk1 served as a loading control. HMW, high-molecular-weight smear.

(B) Fluorescence microscopy of WT cells expressing GFPs with the indicated C-terminal tails. White dashed lines indicate cell boundaries. BF, bright field. Scale bar, 5 μm.

(C) FRAP analysis of GFP-T30 inclusions. Representative images of pre- and post-bleach are shown, with the photobleached area circled. Scale bar, 1 μm. Graph curves represent mean measurements of 10 inclusions, with error bars indicating SEM. Diffuse GFP-T20 was used as a control.

(D) GFPs with C-terminal polythreonine tails were expressed under the *GAL1* promoter in WT cells. Detergent-insoluble aggregates tended to stack within polyacrylamide gel pockets. The aggregates were better resolved using SDD-AGE.

(E) Fluorescence microscopy of GFPs with polythreonine tails as described in (D). Representative inclusions are shown if detectable. Scale bar, 5 μm. The number of cells with GFP inclusions was counted and is represented in the graph as a percentage of GFP-expressing cells. Mean ± SEM from three biological replicates are shown, with more than 150 cells observed for each tail per biological replicate.

(F) FLAG-tagged polythreonine peptides were expressed under the *GAL1* promoter in WT cells. Fixed cells were spheroplasted and subjected to immunofluorescence microscopy using anti-FLAG antibody (α-FLAG). Scale bar, 5 μm.

(G) WT cells expressing FLAG-tagged polythreonine peptides, as described in (F), were lysed and subjected to SDD-AGE and SDS-PAGE, followed by anti-FLAG immunoblotting.

(H) Fluorescence microscopy of WT cells expressing GFPs with polythreonine, polyglutamine, and polyasparagine tails. Scale bar, 5 μm.

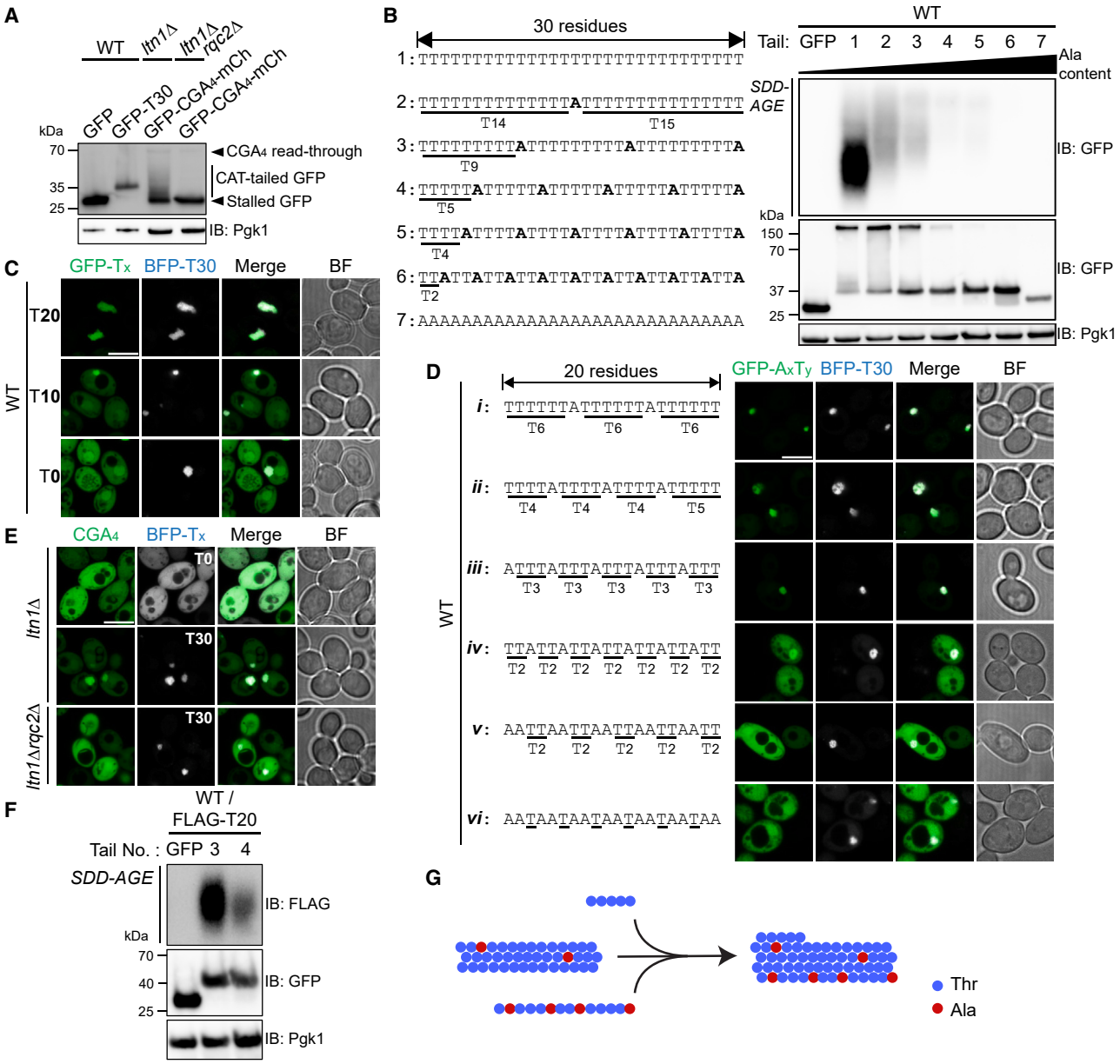

Figure 3. Seeding effect between threonine-rich tails

(A) GFP and GFP-T30 were expressed in WT cells (lanes 1 and 2). The CGA_4 stalling reporter (see Figure 1A) was expressed in *ltn1*Δ and *ltn1*Δ*rqc2*Δ cells (lanes 3 and 4). All constructs were expressed under the *GAL1* promoter. Cell lysates were analyzed by anti-GFP immunoblotting (IB). To achieve comparable levels of IB signal, three times more cell lysates were loaded in lanes 3 and 4 than in lanes 1 and 2. Pgk1 served as a loading control.

(B) Sequences of alanine-interrupted polythreonine tails (tail numbers 1–7) are shown. GFPs fused to each tail were expressed under the *GAL1* promoter in WT cells. Cell lysates were separated by SDD-AGE and SDS-PAGE, followed by anti-GFP immunoblotting.

(C) Fluorescence microscopy of BFP-T30 co-expressed with GFPs containing different lengths of polythreonine tails. BF, bright field. Scale bar, 5 μm.

(D) Sequences of mixed alanine and threonine tails (tail numbers *i*–*vi*) are shown. GFPs fused to each tail (A_xT_y) were co-expressed with BFP-T30 under the *GAL1* promoter in WT cells. Scale bar, 5 μm.

(E) BFP (T0) or BFP-T30 (T30) was co-expressed with the CGA_4 stalling reporter (see Figure 1A) in *ltn1*Δ or *ltn1*Δ*rqc2*Δ cells. Scale bar, 5 μm.

(F) FLAG-T20 (Figure 2G) was co-expressed with GFP or GFPs containing mixed alanine and threonine tails (tail numbers 3 and 4 from B) in WT cells.

(G) Proposed model for CAT tail aggregation.

Nevertheless, it is noteworthy that alanine interruption at a low level was tolerated for polythreonine aggregation, and a tail containing stretches of only five consecutive threonine residues due to alanine interruption still formed detergent-resistant aggregates (Figure 3B, tail 4) and microscopic inclusions (Figure S3A, tail 4).

Previous studies have identified the aggregation propensity of alternating alanine and threonine repeats.[30,31,42] Despite the low threonine content, 15 repeats of the alanine-threonine dipeptide displayed robust aggregation (Figure S3B, compare lanes 2 and 3). The alternating pattern of hydrophobic and hydrophilic residues likely contributes to this high aggregation propensity.[43,44] Unlike other threonine-rich tails that aggregate in the cytosol (Figure S3A), alanine-threonine repeat aggregates were primarily observed in the nucleoplasm (Figures S3C and S3D), outside the nucleolus (Figure S3E). Notably, substituting threonine residues in the repeat with other aggregation-prone residues, such as glutamine and asparagine, abolished aggregation (Figure S3F). Thus, threonine residues are critical for the aggregation of this uniquely patterned sequence. Taken together, our data indicate that Rqc2 can extend CAT tails to lengths capable of aggregation. When these tails exceed a certain threonine content threshold or contain alanine-threonine dipeptide repeats, they can coalesce, driving stalled polypeptide aggregation.

Finally, we examined the potential impact of phosphorylation on polythreonine aggregation. To mimic phospho-threonine, we introduced glutamate residues into 30-residue-long polythreonine tails, which resulted in a substantial reduction in aggregation (Figure S3G). Therefore, phosphorylation of polythreonine stretches would likely interfere with aggregation.

Co-aggregation of heterogeneous threonine-rich tails

We next investigated if aggregation tendency was exclusive to relatively long polythreonine tracts. We were particularly interested in the potential seeding effect of longer tail aggregates on shorter, soluble tails. Accordingly, we co-expressed GFP-T20 and blue fluorescent protein with a C-terminal T30 (BFP-T30). When expressed alone, GFP-T20 was diffusely distributed within cells (Figure 2B). However, upon co-expression with BFP-T30, GFP-T20 was efficiently sequestered to BFP-T30 inclusions, leaving a minimal cytosolic GFP signal (Figure 3C, row 1). This seeding effect was mediated by polythreonine tails, as GFP without a tail was not recruited to BFP-T30 inclusions (Figure 3C, row 3). Surprisingly, even a polythreonine tail as short as 10 residues (GFP-T10) was recruited to BFP-T30 aggregates (Figure 3C, row 2), although the higher background fluorescence suggested a lower seeding efficiency compared with GFP-T20.

We then examined whether this seeding effect was exclusive to homopolymeric threonine sequences. To test this, we designed 20-amino acid-long recombinant CAT tails containing increasing numbers of interrupting alanine residues (Figure 3D). These recombinant CAT tails, which lie within the range of natural CAT tail lengths (Figure 3A), were appended to the C terminus of GFP. When expressed individually, none formed inclusions (Figure S3H). However, when co-expressed with BFP-T30, alanine-interrupted CAT tails, even a tail with only two consecutive threonine residues, were recruited to T30 inclusions (Figure 3D, tail *iv*). Thus, consecutive threonine residues were not critical for seeded aggregation. Instead, the total threonine content of the CAT tail appeared crucial for the interaction with polythreonine seeds. Indeed, as additional alanine residues were introduced, recombinant CAT tails ceased to interact with polythreonine inclusions (Figure 3D, tails *v* and *vi*). Similar to recombinant CAT tails, natural CAT tails appended to stalled GFP were also seeded by BFP-T30 aggregates in *ltn1*Δ cells (Figure 3E, row 2). However, in *ltn1*Δ*rqc2*Δ cells, the same reporter without CAT tails did not interact with polythreonine inclusions (Figure 3E, row 3). In summary, polythreonine inclusions seeded aggregation of both natural and recombinant CAT tails.

Conversely, we investigated whether alanine-interrupted polythreonine aggregates could induce aggregation of short homopolymeric threonine stretches. We used 30-residue-long recombinant CAT tails with stretches of only nine or five consecutive threonines as aggregation seeds (Figure 3B, tails 3 and 4). Interestingly, these alanine-interrupted threonine aggregates templated FLAG-T20 peptides, inducing detergent-resistant smears (Figure 3F). This finding suggests that alanine interruption in both template aggregates and assembling monomeric proteins can be tolerated to some degree during seeded aggregation. Taken together, the ability of threonine-rich protein aggregates to recruit shorter alanine-interrupted stretches likely underlies co-aggregation of heterogeneous natural CAT tails (Figure 3G).

We next examined the seeding capacity of alanine-threonine dipeptide repeat aggregates, a distinctive type of threonine-based aggregate with high alanine content. While these aggregates did recruit other threonine-containing tails, the overall seeding effect was modest (Figure S3I). Furthermore, seeding efficiency did not directly correlate with threonine content. However, alanine-threonine repeats exhibited remarkably pronounced homotypic interactions, sequestering protein tails of the same repeat motif (Figure S3J, row 2). By contrast, polythreonine aggregates demonstrated robust seeding effects across a wide range of threonine-rich tails (compare Figures 3D and S3I), including alanine-threonine dipeptide repeats (Figure S3J, row 3). Overall, our data demonstrate crosstalk between the two threonine-based aggregation motifs, polythreonine and alanine-threonine dipeptide repeats, with polythreonine showing a more dominant effect.

Polythreonine interacts with polyserine

To better understand the structural basis of polythreonine aggregates and their seeding activity, we investigated their interaction with other homopolymeric amino acids. We primarily focused on uncharged hydrophilic amino acids (serine, glutamine, and asparagine) as well as glycine, since polyglycine inclusions are a hallmark of certain neurodegenerative disorders such as fragile X-associated tremor/ataxia syndrome (FXTAS) and neuronal intranuclear inclusion disease (NIID).[45–47] None of the GFP constructs harboring the C-terminal polyamino acid tails mentioned above formed inclusions when the tail length was limited to 30 residues (Figures 2H and 4A). Surprisingly, co-expressed polythreonine inclusions robustly sequestered the polyserine tract (GFP-S30) but not the other examined polyamino acids (Figure 4B). Furthermore, polyserine presented detergent-resistant smears (Figure 4C), indicating stable co-aggregation of BFP-T30 and GFP-S30. Consistent with microscopy (Figures 4A and 4B), GFP-S30 displayed detergent-resistant smears only in the presence of BFP-T30 (Figure 4D). The interaction between polythreonine and polyserine was length-dependent; a 25-residue-long polyserine tail still interacted with polythreonine aggregates, while a 20-residue-long polyserine tail did not (Figures 4E and 4F). Overall, our data highlight

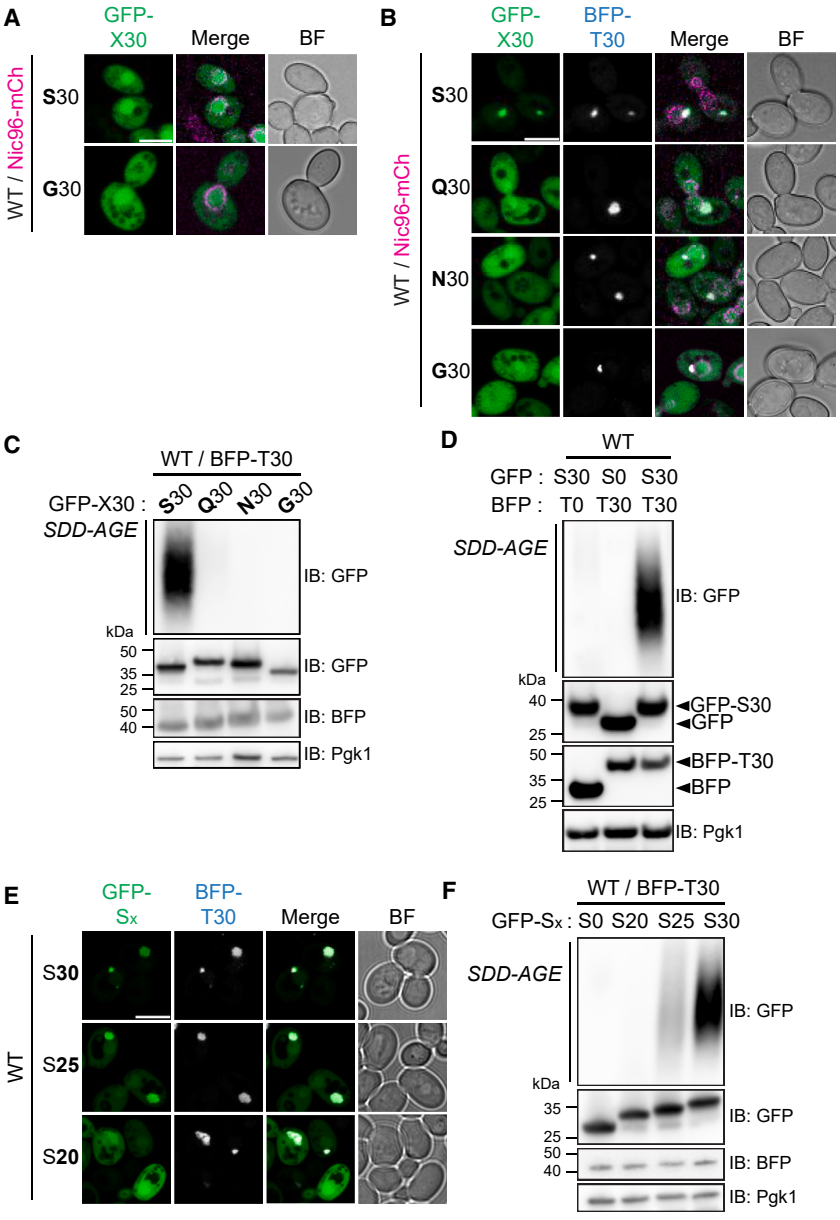

Figure 4. Polythreonine interacts with polyserine

(A and B) Fluorescence microscopy of WT cells expressing GFPs with the indicated polyamino acid tails in the absence (A) or presence (B) of co-expressed BFP-T30. All constructs were expressed under the *GAL1* promoter. Nic96-mCherry, nuclear membrane marker; BF, bright field. Scale bar, 5 μm.

(C) Lysates of cells from (B) were separated using SDD-AGE and SDS-PAGE, followed by anti-GFP and anti-BFP immunoblotting (IB). Pgk1 served as a loading control.

(D) GFP or GFP-S30 was co-expressed with BFP or BFP-T30 in WT cells. The expression of each protein was verified by anti-GFP and anti-BFP immunoblotting.

(E) Fluorescence microscopy of GFPs with varying lengths of polyserine tails, co-expressed with BFP-T30 in WT cells. Scale bar, 5 μm.

(F) Lysates of cells from (E) were analyzed using SDD-AGE and SDS-PAGE. The first lane is a GFP control, co-expressed with BFP-T30.

the specificity of the interaction between polythreonine and polyserine.

Polythreonine aggregation in human cells

Interestingly, the composition of CAT tails varies among different organisms. In humans, CAT tails predominantly consist of alanine,[29,48] suggesting that threonine-mediated CAT tail aggregation may not occur. To investigate whether polythreonine aggregation is specific to yeast and thus facilitates CAT tail aggregation, or if it is a more general phenomenon, we examined the aggregation potential of 30-residue-long homopolymers of alanine, threonine, glutamine, and serine in human cells. Remarkably, the polythreonine tail (GFP-T30) induced distinctive cloud-like inclusions in the cytoplasm across various cell types, including HeLa, HEK293T, and SH-SY5Y (Figures 5A and S4A). By contrast, the other polyamino acids remained diffuse throughout the cells. Notably, even polyglutamine, recognized for its high aggregation propensity, failed to form inclusions at the length of 30 amino acids. FRAP analyses revealed that GFP-T30 was immobile within inclusions, a characteristic of solid-state aggregates like polyglutamine-expanded huntingtin inclusions (Figures 5B and S4B). Consistent with this limited mobility, GFP-T30 in human cells exhibited a detergent-resistant HMW smear (Figure 5C). Polyalanine (GFP-A30) expression level was noticeably lower than the other proteins (Figure 5C), primarily due to its active degradation by proteasomes (Figure S4C). Length-dependent polythreonine aggregation, previously observed in yeast cells (Figures 2D and 2E), was similarly evident in human cells. GFP-T20 did not exhibit detergent-resistant smears and remained diffuse in various cell types (Figures S4D and S4E).

Next, we examined the cross-seeding effect of polythreonine on polyserine in human cells. GFP-S30, a soluble protein in HeLa cells (Figure 5D, second row), formed puncta upon co-expression with BFP-T30 (Figure 5D, third row). The GFP-S30 puncta co-localized with BFP-T30 inclusions. However, BFP-T30 did not recruit GFP without a polyserine tail (Figure 5D, first row), confirming the interaction between polythreonine and polyserine. We conducted FRAP analysis of the inclusions by bleaching only GFP-S30 while preserving BFP-T30 fluorescence (Figure 5E). The limited fluorescence recovery of GFP-S30 suggested its immobility within the inclusion and minimal exchange with free cytosolic GFP-S30. Additionally, co-expression with BFP-T30 intensified the

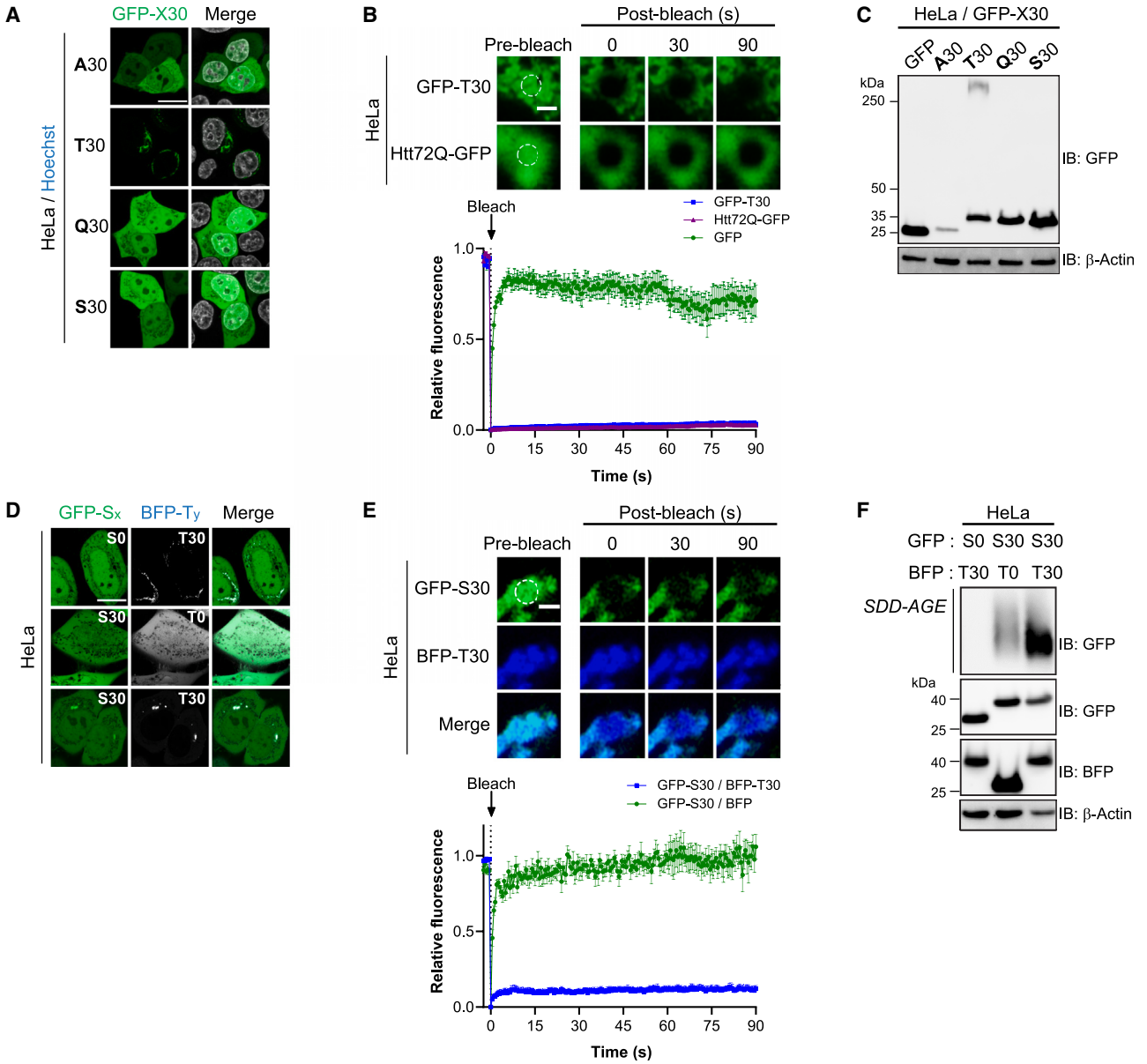

Figure 5. Polythreonine aggregation in human cells

(A) HeLa cells were transfected to express GFPs containing either polyalanine, polythreonine, polyglutamine, or polyserine tails. Nuclei were counterstained with Hoechst and represented in gray in merged images. Scale bar, 15 μm.

(B) FRAP analyses of GFP, GFP-T30, and Htt72Q-GFP (huntingtin exon 1 containing a 72-residue-long polyglutamine tract) in HeLa cells. Representative images of GFP-T30 and Htt72Q-GFP inclusions are shown, with photobleached areas circled. Scale bar, 1 μm. Graph curves represent mean measurements of 10 inclusions, with error bars indicating SEM.

(C) Lysates of HeLa cells expressing GFPs, with or without the indicated polyamino acid tails, were analyzed by anti-GFP immunoblotting (IB). β-actin served as a loading control.

(D) Fluorescence microscopy of GFP or GFP-S30, co-expressed with BFP or BFP-T30 in HeLa cells. Scale bar, 15 μm.

(E) FRAP analyses of GFP-S30 co-localized with BFP-T30 inclusions in HeLa cells. Representative images of inclusions are shown, with the photobleached area circled. Scale bar, 1 μm. Graph curves represent mean measurements of 10 inclusions, with error bars indicating SEM. Diffuse GFP-S30 co-expressed with BFP was used as a control.

(F) Lysates of HeLa cells expressing GFP-S30 (or GFP) and BFP-T30 (or BFP) were analyzed by SDD-AGE and SDS-PAGE.

GFP-S30 smear (Figure 5F), confirming the stable detergent-resistant interaction between polythreonine and polyserine in human cells. Overall, our data suggest that polythreonine aggregation and its cross-seeding on polyserine are general molecular phenomena observed in both yeast and human cells.

Polythreonine aggregates disturb proteostasis

Previous studies in yeast have shown that CAT-tailed stalled polypeptide aggregates sequester various molecular chaperones, prominently including the Hsp40 Sis1.[30–32] Accordingly, we investigated whether polythreonine aggregates also capture Sis1 and other chaperones. Under normal conditions, Sis1 fused to C-terminal mCherry (Sis1-mCh) was mostly localized in the nucleus (Figure S5A). Remarkably, GFP-T30 aggregates sequestered Sis1-mCh in the cytosol (Figure 6A). In sharp contrast, Ydj1, another Hsp40 abundant in the cytosol (Figure S5A), showed poor binding to polythreonine aggregates (Figure 6A), indicating that polythreonine aggregates have varying affinities for different chaperones. To map the polythreonine-interacting domain in Sis1, we expressed Sis1 lacking its C-terminal domain (CTD). Although the CTD is known to bind unfolded protein substrates, it has been shown to be dispensable for cell survival.[49,50] Indeed, mCherry-fused Sis1 lacking the CTD ($Sis1^{\Delta CTD}$-mCh) was sufficient for cell viability in this study (Figures S5B and S5C). Notably, $Sis1^{\Delta CTD}$-mCh did not bind polythreonine aggregates (Figure S5D), suggesting that the CTD is essential for this interaction. We also observed that two major cytosolic Hsp70s, Ssa1 and Ssa2, as well as Hsp104 associate with polythreonine aggregates (Figure 6B). Normally, these chaperones were diffusely distributed in cells (Figure S5E). The sequestration of multiple chaperones by polythreonine aggregates likely disrupts cellular proteostasis, consistent with the increased HSR[51–55] (Figure 6C).

We next investigated whether polythreonine could affect other aggregation-prone proteins. Polyglutamine-expanded huntingtin aggregation in yeast cells requires [*PIN*$^+$] prion,[56,57] an aggregated state of Rnq1 protein (Figure S5F).[58] Indeed, the huntingtin exon 1 fragment containing a 103-residue-long polyglutamine tract and C-terminal GFP (Htt103Q-GFP) formed aggregates only in [*PIN*$^+$] cells but not in [*pin*$^-$] cells (Figure S5G). Remarkably, BFP-T30 in [*pin*$^-$] cells induced both microscopic inclusions (Figure 6D, row 2) and detergent-resistant HMW smears of Htt103Q-GFP (Figure 6E, lane 3). To exclude the possibility of [*PIN*$^+$]/[*pin*$^-$] prion state conversion by polythreonine, we replicated the experiment in cells deleted for *RNQ1*. Notably, BFP-T30 still prompted huntingtin aggregation (Figure S5H), suggesting that the impact of polythreonine on huntingtin aggregation was not mediated by the [*PIN*$^+$] prion.

We then investigated whether polythreonine could also induce huntingtin aggregation in human cells. In HeLa cells, we co-expressed GFP-fused huntingtin exon 1 fragments, containing either a 25- or 46-residue-long polyglutamine tract (Htt25Q-GFP or Htt46Q-GFP), with BFP or BFP-T30. SDD-AGE analysis identified a low basal level of Htt46Q-GFP smear, whereas Htt25Q-GFP aggregation was not detectable (Figure 6F, lanes 1 and 2). Co-expression of BFP-T30 intensified the Htt46Q-GFP smear (Figure 6F, lane 4). Consistently, BFP-T30 aggregates significantly enhanced the formation of Htt46Q-GFP inclusions, while no such effect was observed for Htt25Q-GFP (Figure 6G). In contrast to polyserine, which co-localized with polythreonine aggregates (Figures 4B and 5D), huntingtin tended to form separate aggregates in both yeast and human cells (Figures 6D, 6G, and S5H). Although we cannot exclude the possibility of cross-seeding between polythreonine and huntingtin with $\geq$46Q, it is likely that chaperone sequestration by polythreonine permitted huntingtin aggregation.

DISCUSSION

Although CAT tail-driven stalled polypeptide aggregation in yeast has been consistently observed,[30–32,34,39,59] the heterogeneous nature of CAT tails has posed challenges in understanding their aggregation mechanism. In this study, we manipulated the composition of CAT tails by overexpressing alanyl- and threonyl-tRNAs. Interestingly, $tRNA^{Thr(IGU)}$ enhanced the aggregation of stalled reporters, while $tRNA^{Ala(IGC)}$ conversely attenuated the aggregation. These results provided insights into the mechanism of threonine residue-mediated CAT tail aggregation. Similar approaches may prove useful for investigating CAT tail function and behavior in other organisms. To further dissect the aggregation process, we examined hard-coded CAT tails. Our findings indicate that the formation of nuclei by longer, threonine-enriched CAT tails facilitates the recruitment of shorter CAT tails with lower threonine content, resulting in the growth of stalled polypeptide aggregates.

Notably, polythreonine tracts are underrepresented compared with other hydrophilic amino acid tracts in the human proteome.[60,61] Only three proteins harbor polythreonine stretches longer than 10 amino acids: KDM6B (11 residues), ANK3 (12 residues), and CADM1 (13 residues). It is plausible that polythreonine, being a highly aggregation-prone motif, has been evolutionarily avoided. In the context of this study, mucin-2, a major constituent of colon mucus, is particularly intriguing. Although mucin-2 contains relatively short polythreonine tracts, with a maximum of 8 consecutive residues, these tracts recur multiple times. As a result, threonine constitutes 33% of the ~550 kDa protein. Furthermore, threonine tracts cluster in the central region of mucin-2, constituting >55% of this ~240 kDa domain. Threonine residues in mucin-2 are heavily glycosylated, which likely inhibits aberrant aggregation. However, both commensal and pathogenic gut microbiota can utilize these glycan chains as a nutrient source.[62,63] Whether deglycosylated and/or unglycosylated threonine residues in mucin-2 could induce aggregation, and if so, its impact on physiological mucus turnover, as well as infection and inflammation, would be intriguing questions.

Surprisingly, polythreonine displayed a cross-seeding effect on polyserine (Figures 4 and 5D–5F). Notably, a recent report revealed the formation of cytosolic assemblies by 42-residue-long polyserine tracts in human cells.[64] The report also demonstrated that microscopic polyserine assemblies can serve as sites for tau aggregation, potentially linking polyserine to Alzheimer's disease and tauopathies. The interaction between polythreonine and polyserine observed in this study suggests a potential commonality in their structural elements. The relationship between polythreonine and polyserine is similar to that between polyglutamine and polyasparagine, both of which are aggregation-prone motifs with amide groups in their side chains.[65–69] In this regard, hydroxyl groups in the side chains of polythreonine and polyserine could align in a way that confers structural stability. Unlike polythreonine, polyserine tracts are more prevalent in the human proteome.[60,61] However, most of them consist of 25 residues or fewer,

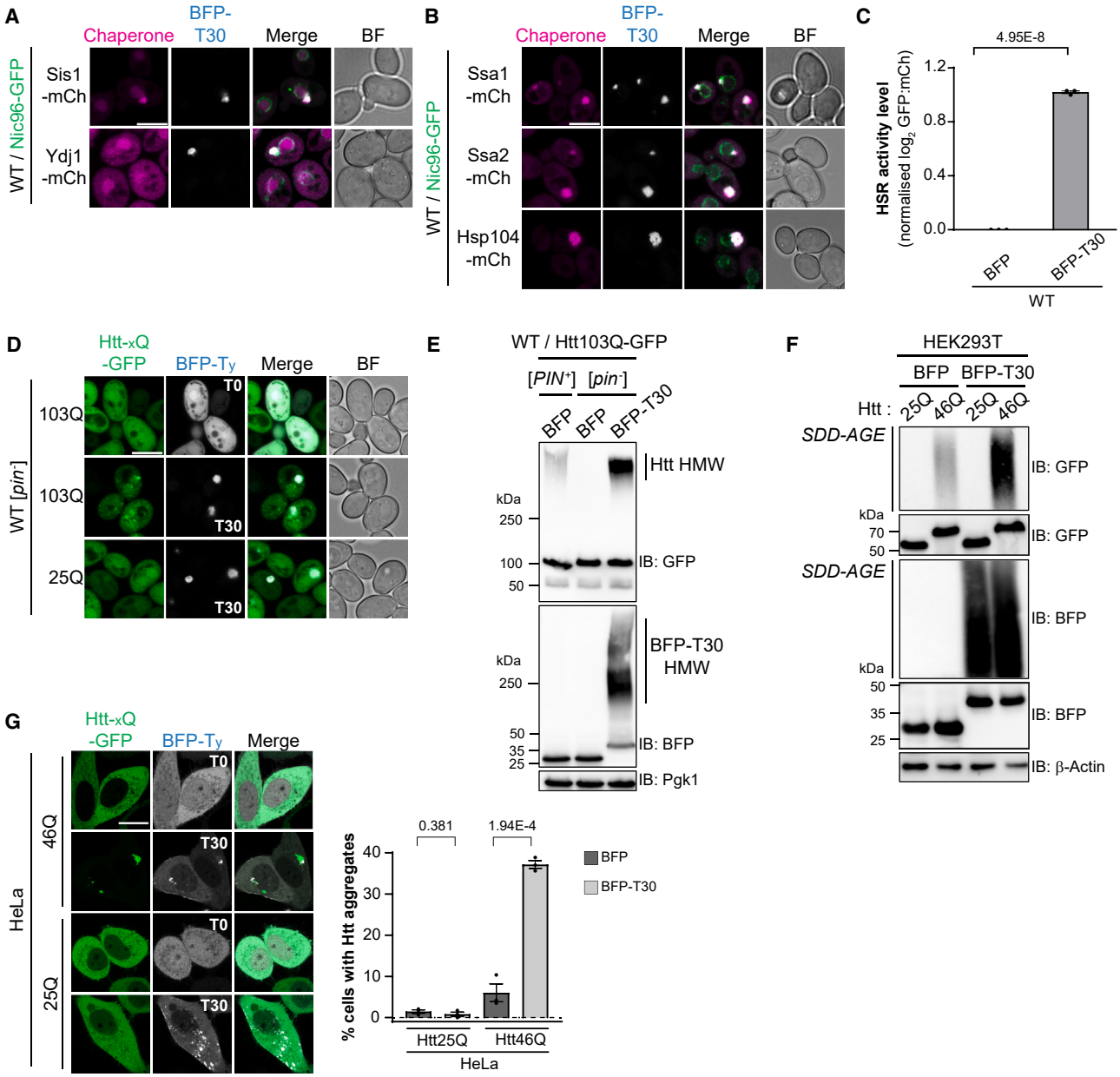

Figure 6. Polythreonine aggregates disturb proteostasis

(A and B) BFP-T30 was expressed under the *GAL1* promoter in cells with the indicated chaperone genes fused to C-terminal mCherry. Nic96-GFP, nuclear marker; BF, bright field. Scale bar, 5 μm.

(C) BFP and BFP-T30 were expressed under the *GAL1* promoter in WT cells containing the HSR reporter (see Figure 1F). Cells cultured at 25°C were analyzed using flow cytometry. Black dot, individual data point; error bar, SEM ($n = 3$). p value was calculated using Student's t test (unpaired, two-tailed).

(D) GFP-fused huntingtin exon1 (25Q or 103Q) was co-expressed with BFP or BFP-T30 in WT [*pin*$^-$] cells. All constructs were expressed under the *GAL1* promoter. Scale bar, 5 μm.

(E) Htt103Q-GFP was co-expressed with either BFP or BFP-T30 in [*PIN*$^+$] and [*pin*$^-$] cells as indicated. Cell lysates were analyzed by anti-GFP and anti-BFP immunoblotting (IB). HMW, high-molecular-weight smear. Pgk1 served as a loading control.

(F and G) GFP-fused huntingtin exon 1 (25Q or 46Q) was co-expressed with BFP or BFP-T30 in HEK293T cells (F) for immunoblotting and in HeLa cells (G) for microscopy analyses. Scale bar, 15 μm. (G) Cells with huntingtin inclusions were counted and presented as a percentage of GFP-expressing cells, with means ± SEM from three biological replicates. Over 100 GFP-positive cells were counted per condition in each experiment. p values were obtained by one-way ANOVA.

rendering them unlikely to form aggregates under physiological conditions. The aggregation potential of three outlier polyserine tracts in the human proteome remains to be investigated: TNRC18 (58 residues), MLLT3 (42 residues), and SRRM2 (42 residues). Among these, SRRM2 stands out as a potential candidate for aggregation, given its high local concentration within cytosolic and nuclear bio-condensates.[64] SRRM2 functions as one of the two scaffolding proteins of the nuclear speckle,[70,71] a membraneless organelle associated with mRNA metabolism.[72] It would be intriguing to investigate whether the liquid/solid state of SRRM2, and consequently the dynamics of nuclear speckles, could be regulated by their associated RNAs and potential phosphorylation of the polyserine tract.

Why does the yeast CAT tail contain threonine residues if threonine-rich tracts are prone to aggregation? CAT tail composition has been analyzed in three eukaryotes and one prokaryote: yeast, fruit flies, humans, and *Bacillus subtilis*.[22,29,42,48,73] Interestingly, each organism displays a distinct CAT tail composition. In fruit flies, CAT tails contain alanine, threonine, and possibly a few other amino acids,[42] whereas in humans and *B. subtilis*, CAT tails are primarily composed of alanine.[29,48,73] Thus, humans may avoid proteotoxic threonine-driven CAT tail aggregation, which can be particularly detrimental in terminally differentiated, non-dividing cells such as neurons since polythreonine can induce secondary aggregation of other proteins such as huntingtin (Figures 6D–6G). By contrast, CAT tail aggregation could be advantageous for yeast, a single-celled, fast-dividing organism. CAT tail aggregation could function as a mechanism to collect potentially toxic stalled polypeptides produced in excess under stress conditions.[74–76] In actively dividing cells, CAT tail aggregates could be asymmetrically segregated to mother cells, thereby alleviating the proteotoxic burden in daughter cells.[77–79] Moreover, threonine-based CAT tail aggregates, unlike other pathogenic protein aggregates, do not interfere with the HSR (Figure 6C), allowing cells to cope with stress.[80–83] Thus, acute translation stress and consequent CAT tail aggregation may be tolerable in yeast, although chronic aggregation of stalled polypeptides during aging results in declining proteostasis.[34]

Limitations of the study

The structural basis of polythreonine aggregation requires further investigation, but several lines of evidence suggest amyloid-like aggregation. Firstly, the aggregates displayed remarkable stability, resisting detergent—a characteristic often attributed to the cross-β structure of amyloids.[84–87] Secondly, polythreonine aggregates effectively sequestered other proteins with similar sequences, reminiscent of the seeding ability observed in amyloid fibrils.[88,89] Lastly, polythreonine longer than 70 residues has been shown to form fibrillar structures *in vitro*.[90] Although the report proposed that polypeptide backbones possess a generic aggregation tendency, our study highlights the exceptional robustness of polythreonine aggregation *in vivo*, underscoring the significance of polythreonine side chains in driving aggregation. However, it is unlikely that a highly heterogeneous CAT tail population would form an ordered structure upon aggregation. Instead, it is tempting to speculate that local interactions between threonine patches drive the formation of amorphous yet highly stable aggregates. Elucidating the physicochemical basis of threonine-rich polypeptide assembly will provide deeper insights into the initiation and progression of CAT tail aggregation.

RESOURCE AVAILABILITY

Lead contact

Further information and requests for resources and reagents should be directed to and will be fulfilled by the lead contact, Young-Jun Choe (yjchoe@ntu.edu.sg).

Materials availability

Plasmids and yeast strains generated in this study will be available from the lead contact upon request.

Data and code availability

- Original imaging data have been deposited at Mendeley and are publicly available as of the date of publication. The DOI is listed in the key resources table.
- This paper does not report any original code.
- Any additional information required to reanalyze the data reported in this paper is available from the lead contact upon request.

ACKNOWLEDGMENTS

We thank Soak Kuan Lai and Abdul Rashid (Nanyang Technological University) for their guidance in confocal microscopy and flow cytometry, respectively. We appreciate John Schulze (University of California, Davis, USA) for performing the amino acid analysis at the UC Davis Genome Center Molecular Structure Facility. We also thank Xavier Roca and I-Hsin Su (Nanyang Technological University) for providing human cell lines and access to equipment. This research is supported by the Nanyang Technological University, Singapore, under its Nanyang Assistant Professorship Start-Up Grant (Y.-J.C.) and the Ministry of Education – Singapore under its Academic Research Fund Tier 1 (project ID RG28/22; Y.-J.C.).

AUTHOR CONTRIBUTIONS

Conceptualization, Y.-J.C.; methodology, W.D.C., M.-J.Y., and Y.-J.C.; investigation, W.D.C., M.-J.Y., K.H.Y., and Y.-J.C.; writing—original draft, Y.-J.C.; writing—review & editing, W.D.C., M.-J.Y., and Y.-J.C.; funding acquisition, Y.-J.C.; resources, W.D.C. and M.-J.Y.; supervision, Y.-J.C.

DECLARATION OF INTERESTS

The authors declare no competing interests.

STAR★METHODS

Detailed methods are provided in the online version of this paper and include the following:

- KEY RESOURCES TABLE
- EXPERIMENTAL MODEL AND STUDY PARTICIPANT DETAILS
  - Yeast strains
  - Human cell lines
- METHOD DETAILS
  - Yeast culture and transformation
  - Plasmid design
  - Mammalian cell culture and transfection
  - Yeast lysate preparation
  - Immunoprecipitation
  - Mammalian cell lysate preparation
  - Immunoblotting
  - Northern blot for yeast tRNA
  - Amino acid analysis

- Fluorescence microscopy
- Live-cell FRAP
- Yeast immunofluorescence microscopy
- Spotting growth assay
- Flow cytometry

- QUANTIFICATION AND STATISTICAL ANALYSIS

SUPPLEMENTAL INFORMATION

Supplemental information can be found online at https://doi.org/10.1016/j.molcel.2024.10.011.

Received: February 26, 2024
Revised: August 1, 2024
Accepted: October 9, 2024
Published: November 1, 2024

REFERENCES

1. Frischmeyer, P.A., van Hoof, A., O'Donnell, K., Guerrerio, A.L., Parker, R., and Dietz, H.C. (2002). An mRNA surveillance mechanism that eliminates transcripts lacking termination codons. Science *295*, 2258–2261. https://doi.org/10.1126/science.1067338.
2. Yan, L.L., Simms, C.L., McLoughlin, F., Vierstra, R.D., and Zaher, H.S. (2019). Oxidation and alkylation stresses activate ribosome-quality control. Nat. Commun. *10*, 5611. https://doi.org/10.1038/s41467-019-13579-3.
3. Wu, C.C.C., Peterson, A., Zinshteyn, B., Regot, S., and Green, R. (2020). Ribosome Collisions Trigger General Stress Responses to Regulate Cell Fate. Cell *182*, 404–416.e14. https://doi.org/10.1016/j.cell.2020.06.006.
4. Zhao, S., Cordes, J., Caban, K.M., Götz, M.J., Mackens-Kiani, T., Veltri, A.J., Sinha, N.K., Weickert, P., Kaya, S., Hewitt, G., et al. (2023). RNF14-dependent atypical ubiquitylation promotes translation-coupled resolution of RNA-protein crosslinks. Mol. Cell *83*, 4290–4303.e9. https://doi.org/10.1016/j.molcel.2023.10.012.
5. Schuller, A.P., and Green, R. (2018). Roadblocks and resolutions in eukaryotic translation. Nat. Rev. Mol. Cell Biol. *19*, 526–541. https://doi.org/10.1038/s41580-018-0011-4.
6. Inada, T. (2020). Quality controls induced by aberrant translation. Nucleic Acids Res. *48*, 1084–1096. https://doi.org/10.1093/nar/gkz1201.
7. Brandman, O., and Hegde, R.S. (2016). Ribosome-associated protein quality control. Nat. Struct. Mol. Biol. *23*, 7–15. https://doi.org/10.1038/nsmb.3147.
8. Joazeiro, C.A.P. (2019). Mechanisms and functions of ribosome-associated protein quality control. Nat. Rev. Mol. Cell Biol. *20*, 368–383. https://doi.org/10.1038/s41580-019-0118-2.
9. Sitron, C.S., and Brandman, O. (2020). Detection and Degradation of Stalled Nascent Chains via Ribosome-Associated Quality Control. Annu. Rev. Biochem. *89*, 417–442. https://doi.org/10.1146/annurev-biochem-013118-110729.
10. Simms, C.L., Yan, L.L., and Zaher, H.S. (2017). Ribosome Collision Is Critical for Quality Control during No-Go Decay. Mol. Cell *68*, 361–373.e5. https://doi.org/10.1016/j.molcel.2017.08.019.
11. Meydan, S., and Guydosh, N.R. (2020). Disome and Trisome Profiling Reveal Genome-wide Targets of Ribosome Quality Control. Mol. Cell *79*, 588–602.e6. https://doi.org/10.1016/j.molcel.2020.06.010.
12. Matsuo, Y., Ikeuchi, K., Saeki, Y., Iwasaki, S., Schmidt, C., Udagawa, T., Sato, F., Tsuchiya, H., Becker, T., Tanaka, K., et al. (2017). Ubiquitination of stalled ribosome triggers ribosome-associated quality control. Nat. Commun. *8*, 159. https://doi.org/10.1038/s41467-017-00188-1.
13. Juszkiewicz, S., and Hegde, R.S. (2017). Initiation of Quality Control during Poly(A) Translation Requires Site-Specific Ribosome Ubiquitination. Mol. Cell *65*, 743–750.e4. https://doi.org/10.1016/j.molcel.2016.11.039.
14. Juszkiewicz, S., Chandrasekaran, V., Lin, Z., Kraatz, S., Ramakrishnan, V., and Hegde, R.S. (2018). ZNF598 Is a Quality Control Sensor of Collided Ribosomes. Mol. Cell *72*, 469–481.e7. https://doi.org/10.1016/j.molcel.2018.08.037.
15. Ikeuchi, K., Tesina, P., Matsuo, Y., Sugiyama, T., Cheng, J., Saeki, Y., Tanaka, K., Becker, T., Beckmann, R., and Inada, T. (2019). Collided ribosomes form a unique structural interface to induce Hel2-driven quality control pathways. EMBO J. *38*, e100276. https://doi.org/10.15252/embj.2018100276.
16. Juszkiewicz, S., Speldewinde, S.H., Wan, L., Svejstrup, J.Q., and Hegde, R.S. (2020). The ASC-1 Complex Disassembles Collided Ribosomes. Mol. Cell *79*, 603–614.e8. https://doi.org/10.1016/j.molcel.2020.06.006.
17. Matsuo, Y., Tesina, P., Nakajima, S., Mizuno, M., Endo, A., Buschauer, R., Cheng, J., Shounai, O., Ikeuchi, K., Saeki, Y., et al. (2020). RQT complex dissociates ribosomes collided on endogenous RQC substrate SDD1. Nat. Struct. Mol. Biol. *27*, 323–332. https://doi.org/10.1038/s41594-020-0393-9.
18. Narita, M., Denk, T., Matsuo, Y., Sugiyama, T., Kikuguchi, C., Ito, S., Sato, N., Suzuki, T., Hashimoto, S., Machová, I., et al. (2022). A distinct mammalian disome collision interface harbors K63-linked polyubiquitination of uS10 to trigger hRQT-mediated subunit dissociation. Nat. Commun. *13*, 6411. https://doi.org/10.1038/s41467-022-34097-9.
19. Matsuo, Y., Uchihashi, T., and Inada, T. (2023). Decoding of the ubiquitin code for clearance of colliding ribosomes by the RQT complex. Nat. Commun. *14*, 79. https://doi.org/10.1038/s41467-022-35608-4.
20. Best, K., Ikeuchi, K., Kater, L., Best, D., Musial, J., Matsuo, Y., Berninghausen, O., Becker, T., Inada, T., and Beckmann, R. (2023). Structural basis for clearing of ribosome collisions by the RQT complex. Nat. Commun. *14*, 921. https://doi.org/10.1038/s41467-023-36230-8.
21. Shao, S., Brown, A., Santhanam, B., and Hegde, R.S. (2015). Structure and assembly pathway of the ribosome quality control complex. Mol. Cell *57*, 433–444. https://doi.org/10.1016/j.molcel.2014.12.015.
22. Shen, P.S., Park, J., Qin, Y., Li, X., Parsawar, K., Larson, M.H., Cox, J., Cheng, Y., Lambowitz, A.M., Weissman, J.S., et al. (2015). Protein synthesis. Rqc2p and 60S ribosomal subunits mediate mRNA-independent elongation of nascent chains. Science *347*, 75–78. https://doi.org/10.1126/science.1259724.
23. Bengtson, M.H., and Joazeiro, C.A.P. (2010). Role of a ribosome-associated E3 ubiquitin ligase in protein quality control. Nature *467*, 470–473. https://doi.org/10.1038/nature09371.
24. Osuna, B.A., Howard, C.J., Kc, S., Frost, A., and Weinberg, D.E. (2017). In vitro analysis of RQC activities provides insights into the mechanism and function of CAT tailing. eLife *6*, e27949. https://doi.org/10.7554/eLife.27949.
25. Howard, C.J., and Frost, A. (2021). Ribosome-associated quality control and CAT tailing. Crit. Rev. Biochem. Mol. Biol. *56*, 603–620. https://doi.org/10.1080/10409238.2021.1938507.
26. Tesina, P., Ebine, S., Buschauer, R., Thoms, M., Matsuo, Y., Inada, T., and Beckmann, R. (2023). Molecular basis of eIF5A-dependent CAT tailing in eukaryotic ribosome-associated quality control. Mol. Cell *83*, 607–621.e4. https://doi.org/10.1016/j.molcel.2023.01.020.
27. Kostova, K.K., Hickey, K.L., Osuna, B.A., Hussmann, J.A., Frost, A., Weinberg, D.E., and Weissman, J.S. (2017). CAT-tailing as a fail-safe mechanism for efficient degradation of stalled nascent polypeptides. Science *357*, 414–417. https://doi.org/10.1126/science.aam7787.
28. Sitron, C.S., and Brandman, O. (2019). CAT tails drive degradation of stalled polypeptides on and off the ribosome. Nat. Struct. Mol. Biol. *26*, 450–459. https://doi.org/10.1038/s41594-019-0230-1.
29. Thrun, A., Garzia, A., Kigoshi-Tansho, Y., Patil, P.R., Umbaugh, C.S., Dallinger, T., Liu, J., Kreger, S., Patrizi, A., Cox, G.A., et al. (2021). Convergence of mammalian RQC and C-end rule proteolytic pathways via alanine tailing. Mol. Cell *81*, 2112–2122.e7. https://doi.org/10.1016/j.molcel.2021.03.004.

30. Choe, Y.J., Park, S.H., Hassemer, T., Körner, R., Vincenz-Donnelly, L., Hayer-Hartl, M., and Hartl, F.U. (2016). Failure of RQC machinery causes protein aggregation and proteotoxic stress. Nature *531*, 191–195. https://doi.org/10.1038/nature16973.

31. Yonashiro, R., Tahara, E.B., Bengtson, M.H., Khokhrina, M., Lorenz, H., Chen, K.C., Kigoshi-Tansho, Y., Savas, J.N., Yates, J.R., Kay, S.A., et al. (2016). The Rqc2/Tae2 subunit of the ribosome-associated quality control (RQC) complex marks ribosome-stalled nascent polypeptide chains for aggregation. eLife *5*, e11794. https://doi.org/10.7554/eLife.11794.

32. Defenouillère, Q., Zhang, E., Namane, A., Mouaikel, J., Jacquier, A., and Fromont-Racine, M. (2016). Rqc1 and Ltn1 Prevent C-terminal Alanine-Threonine Tail (CAT-tail)-induced Protein Aggregation by Efficient Recruitment of Cdc48 on Stalled 60S Subunits. J. Biol. Chem. *291*, 12245–12253. https://doi.org/10.1074/jbc.M116.722264.

33. Brandman, O., Stewart-Ornstein, J., Wong, D., Larson, A., Williams, C.C., Li, G.W., Zhou, S., King, D., Shen, P.S., Weibezahn, J., et al. (2012). A ribosome-bound quality control complex triggers degradation of nascent peptides and signals translation stress. Cell *151*, 1042–1054. https://doi.org/10.1016/j.cell.2012.10.044.

34. Stein, K.C., Morales-Polanco, F., van der Lienden, J., Rainbolt, T.K., and Frydman, J. (2022). Ageing exacerbates ribosome pausing to disrupt co-translational proteostasis. Nature *601*, 637–642. https://doi.org/10.1038/s41586-021-04295-4.

35. Letzring, D.P., Wolf, A.S., Brule, C.E., and Grayhack, E.J. (2013). Translation of CGA codon repeats in yeast involves quality control components and ribosomal protein L1. RNA *19*, 1208–1217. https://doi.org/10.1261/rna.039446.113.

36. Chandrasekaran, V., Juszkiewicz, S., Choi, J., Puglisi, J.D., Brown, A., Shao, S., Ramakrishnan, V., and Hegde, R.S. (2019). Mechanism of ribosome stalling during translation of a poly(A) tail. Nat. Struct. Mol. Biol. *26*, 1132–1140. https://doi.org/10.1038/s41594-019-0331-x.

37. Tesina, P., Lessen, L.N., Buschauer, R., Cheng, J., Wu, C.C.C., Berninghausen, O., Buskirk, A.R., Becker, T., Beckmann, R., and Green, R. (2020). Molecular mechanism of translational stalling by inhibitory codon combinations and poly(A) tracts. EMBO J. *39*, e103365. https://doi.org/10.15252/embj.2019103365.

38. Kryndushkin, D.S., Alexandrov, I.M., Ter-Avanesyan, M.D., and Kushnirov, V.V. (2003). Yeast [PSI+] prion aggregates are formed by small Sup35 polymers fragmented by Hsp104. J. Biol. Chem. *278*, 49636–49643. https://doi.org/10.1074/jbc.M307996200.

39. Sitron, C.S., Park, J.H., Giafaglione, J.M., and Brandman, O. (2020). Aggregation of CAT tails blocks their degradation and causes proteotoxicity in S. cerevisiae. PLoS One *15*, e0227841. https://doi.org/10.1371/journal.pone.0227841.

40. Saric, T., Graef, C.I., and Goldberg, A.L. (2004). Pathway for degradation of peptides generated by proteasomes: a key role for thimet oligopeptidase and other metallopeptidases. J. Biol. Chem. *279*, 46723–46732. https://doi.org/10.1074/jbc.M406537200.

41. Beninga, J., Rock, K.L., and Goldberg, A.L. (1998). Interferon-gamma can stimulate post-proteasomal trimming of the N terminus of an antigenic peptide by inducing leucine aminopeptidase. J. Biol. Chem. *273*, 18734–18742. https://doi.org/10.1074/jbc.273.30.18734.

42. Wu, Z., Tantray, I., Lim, J., Chen, S., Li, Y., Davis, Z., Sitron, C., Dong, J., Gispert, S., Auburger, G., et al. (2019). MISTERMINATE Mechanistically Links Mitochondrial Dysfunction with Proteostasis Failure. Mol. Cell *75*, 835–848.e8. https://doi.org/10.1016/j.molcel.2019.06.031.

43. Xiong, H., Buckwalter, B.L., Shieh, H.M., and Hecht, M.H. (1995). Periodicity of polar and nonpolar amino acids is the major determinant of secondary structure in self-assembling oligomeric peptides. Proc. Natl. Acad. Sci. USA *92*, 6349–6353. https://doi.org/10.1073/pnas.92.14.6349.

44. West, M.W., Wang, W., Patterson, J., Mancias, J.D., Beasley, J.R., and Hecht, M.H. (1999). De novo amyloid proteins from designed combinatorial libraries. Proc. Natl. Acad. Sci. USA *96*, 11211–11216. https://doi.org/10.1073/pnas.96.20.11211.

45. Boivin, M., Deng, J., Pfister, V., Grandgirard, E., Oulad-Abdelghani, M., Morlet, B., Ruffenach, F., Negroni, L., Koebel, P., Jacob, H., et al. (2021). Translation of GGC repeat expansions into a toxic polyglycine protein in NIID defines a novel class of human genetic disorders: the polyG diseases. Neuron *109*, 1825–1835.e5. https://doi.org/10.1016/j.neuron.2021.03.038.

46. Todd, P.K., Oh, S.Y., Krans, A., He, F., Sellier, C., Frazer, M., Renoux, A.J., Chen, K.C., Scaglione, K.M., Basrur, V., et al. (2013). CGG repeat-associated translation mediates neurodegeneration in fragile X tremor ataxia syndrome. Neuron *78*, 440–455. https://doi.org/10.1016/j.neuron.2013.03.026.

47. Sellier, C., Buijsen, R.A.M., He, F., Natla, S., Jung, L., Tropel, P., Gaucherot, A., Jacobs, H., Meziane, H., Vincent, A., et al. (2017). Translation of Expanded CGG Repeats into FMRpolyG Is Pathogenic and May Contribute to Fragile X Tremor Ataxia Syndrome. Neuron *93*, 331–347. https://doi.org/10.1016/j.neuron.2016.12.016.

48. Udagawa, T., Seki, M., Okuyama, T., Adachi, S., Natsume, T., Noguchi, T., Matsuzawa, A., and Inada, T. (2021). Failure to Degrade CAT-Tailed Proteins Disrupts Neuronal Morphogenesis and Cell Survival. Cell Rep. *34*, 108599. https://doi.org/10.1016/j.celrep.2020.108599.

49. Kampinga, H.H., and Craig, E.A. (2010). The HSP70 chaperone machinery: J proteins as drivers of functional specificity. Nat. Rev. Mol. Cell Biol. *11*, 579–592. https://doi.org/10.1038/nrm2941.

50. Yan, W., and Craig, E.A. (1999). The glycine-phenylalanine-rich region determines the specificity of the yeast Hsp40 Sis1. Mol. Cell. Biol. *19*, 7751–7758. https://doi.org/10.1128/MCB.19.11.7751.

51. Kmiecik, S.W., and Mayer, M.P. (2022). Molecular mechanisms of heat shock factor 1 regulation. Trends Biochem. Sci. *47*, 218–234. https://doi.org/10.1016/j.tibs.2021.10.004.

52. Masser, A.E., Kang, W., Roy, J., Mohanakrishnan Kaimal, J., Quintana-Cordero, J., Friedländer, M.R., and Andréasson, C. (2019). Cytoplasmic protein misfolding titrates Hsp70 to activate nuclear Hsf1. eLife *8*, e47791. https://doi.org/10.7554/eLife.47791.

53. Zheng, X., Krakowiak, J., Patel, N., Beyzavi, A., Ezike, J., Khalil, A.S., and Pincus, D. (2016). Dynamic control of Hsf1 during heat shock by a chaperone switch and phosphorylation. eLife *5*, e18638. https://doi.org/10.7554/eLife.18638.

54. Krakowiak, J., Zheng, X., Patel, N., Feder, Z.A., Anandhakumar, J., Valerius, K., Gross, D.S., Khalil, A.S., and Pincus, D. (2018). Hsf1 and Hsp70 constitute a two-component feedback loop that regulates the yeast heat shock response. eLife *7*, e31668. https://doi.org/10.7554/eLife.31668.

55. Feder, Z.A., Ali, A., Singh, A., Krakowiak, J., Zheng, X., Bindokas, V.P., Wolfgeher, D., Kron, S.J., and Pincus, D. (2021). Subcellular localization of the J-protein Sis1 regulates the heat shock response. J. Cell Biol. *220*. https://doi.org/10.1083/jcb.202005165.

56. Meriin, A.B., Zhang, X., He, X., Newnam, G.P., Chernoff, Y.O., and Sherman, M.Y. (2002). Huntington toxicity in yeast model depends on polyglutamine aggregation mediated by a prion-like protein Rnq1. J. Cell Biol. *157*, 997–1004. https://doi.org/10.1083/jcb.200112104.

57. Gropp, M.H.M., Klaips, C.L., and Hartl, F.U. (2022). Formation of toxic oligomers of polyQ-expanded Huntingtin by prion-mediated cross-seeding. Mol. Cell *82*, 4290–4306.e11. https://doi.org/10.1016/j.molcel.2022.09.031.

58. Sondheimer, N., and Lindquist, S. (2000). Rnq1: an epigenetic modifier of protein function in yeast. Mol. Cell *5*, 163–172. https://doi.org/10.1016/s1097-2765(00)80412-8.

59. Izawa, T., Park, S.H., Zhao, L., Hartl, F.U., and Neupert, W. (2017). Cytosolic Protein Vms1 Links Ribosome Quality Control to Mitochondrial and Cellular Homeostasis. Cell *171*, 890–903.e18. https://doi.org/10.1016/j.cell.2017.10.002.

60. Lobanov, M.Y., Sokolovskiy, I.V., and Galzitskaya, O.V. (2014). HRaP: database of occurrence of HomoRepeats and patterns in proteomes. Nucleic Acids Res. *42*, D273–D278. https://doi.org/10.1093/nar/gkt927.

61. Kumar, A.S., Sowpati, D.T., and Mishra, R.K. (2016). Single Amino Acid Repeats in the Proteome World: Structural, Functional, and Evolutionary Insights. PLoS One *11*, e0166854. https://doi.org/10.1371/journal.pone.0166854.

62. Hansson, G.C. (2020). Mucins and the Microbiome. Annu. Rev. Biochem. *89*, 769–793. https://doi.org/10.1146/annurev-biochem-011520-105053.

63. McGuckin, M.A., Lindén, S.K., Sutton, P., and Florin, T.H. (2011). Mucin dynamics and enteric pathogens. Nat. Rev. Microbiol. *9*, 265–278. https://doi.org/10.1038/nrmicro2538.

64. Lester, E., Van Alstyne, M., McCann, K.L., Reddy, S., Cheng, L.Y., Kuo, J., Pratt, J., and Parker, R. (2023). Cytosolic condensates rich in polyserine define subcellular sites of tau aggregation. Proc. Natl. Acad. Sci. USA *120*, e2217759120. https://doi.org/10.1073/pnas.2217759120.

65. Lu, X., and Murphy, R.M. (2015). Asparagine Repeat Peptides: Aggregation Kinetics and Comparison with Glutamine Repeats. Biochemistry *54*, 4784–4794. https://doi.org/10.1021/acs.biochem.5b00644.

66. DePace, A.H., Santoso, A., Hillner, P., and Weissman, J.S. (1998). A critical role for amino-terminal glutamine/asparagine repeats in the formation and propagation of a yeast prion. Cell *93*, 1241–1252. https://doi.org/10.1016/s0092-8674(00)81467-1.

67. Osherovich, L.Z., and Weissman, J.S. (2001). Multiple Gln/Asn-rich prion domains confer susceptibility to induction of the yeast [PSI(+)] prion. Cell *106*, 183–194. https://doi.org/10.1016/s0092-8674(01)00440-8.

68. Alberti, S., Halfmann, R., King, O., Kapila, A., and Lindquist, S. (2009). A systematic survey identifies prions and illuminates sequence features of prionogenic proteins. Cell *137*, 146–158. https://doi.org/10.1016/j.cell.2009.02.044.

69. Halfmann, R., Alberti, S., Krishnan, R., Lyle, N., O'Donnell, C.W., King, O.D., Berger, B., Pappu, R.V., and Lindquist, S. (2011). Opposing effects of glutamine and asparagine govern prion formation by intrinsically disordered proteins. Mol. Cell *43*, 72–84. https://doi.org/10.1016/j.molcel.2011.05.013.

70. Ilik, İ.A., Malszycki, M., Lübke, A.K., Schade, C., Meierhofer, D., and Aktaş, T. (2020). SON and SRRM2 are essential for nuclear speckle formation. eLife *9*, e60579. https://doi.org/10.7554/eLife.60579.

71. Xu, S., Lai, S.K., Sim, D.Y., Ang, W.S.L., Li, H.Y., and Roca, X. (2022). SRRM2 organizes splicing condensates to regulate alternative splicing. Nucleic Acids Res. *50*, 8599–8614. https://doi.org/10.1093/nar/gkac669.

72. Galganski, L., Urbanek, M.O., and Krzyzosiak, W.J. (2017). Nuclear speckles: molecular organization, biological function and role in disease. Nucleic Acids Res. *45*, 10350–10368. https://doi.org/10.1093/nar/gkx759.

73. Lytvynenko, I., Paternoga, H., Thrun, A., Balke, A., Müller, T.A., Chiang, C.H., Nagler, K., Tsaprailis, G., Anders, S., Bischofs, I., et al. (2019). Alanine Tails Signal Proteolysis in Bacterial Ribosome-Associated Quality Control. Cell *178*, 76–90.e22. https://doi.org/10.1016/j.cell.2019.05.002.

74. Escusa-Toret, S., Vonk, W.I.M., and Frydman, J. (2013). Spatial sequestration of misfolded proteins by a dynamic chaperone pathway enhances cellular fitness during stress. Nat. Cell Biol. *15*, 1231–1243. https://doi.org/10.1038/ncb2838.

75. Miller, S.B.M., Mogk, A., and Bukau, B. (2015). Spatially organized aggregation of misfolded proteins as cellular stress defense strategy. J. Mol. Biol. *427*, 1564–1574. https://doi.org/10.1016/j.jmb.2015.02.006.

76. Sontag, E.M., Samant, R.S., and Frydman, J. (2017). Mechanisms and Functions of Spatial Protein Quality Control. Annu. Rev. Biochem. *86*, 97–122. https://doi.org/10.1146/annurev-biochem-060815-014616.

77. Aguilaniu, H., Gustafsson, L., Rigoulet, M., and Nyström, T. (2003). Asymmetric inheritance of oxidatively damaged proteins during cytokinesis. Science *299*, 1751–1753. https://doi.org/10.1126/science.1080418.

78. Liu, B., Larsson, L., Caballero, A., Hao, X., Oling, D., Grantham, J., and Nyström, T. (2010). The polarisome is required for segregation and retrograde transport of protein aggregates. Cell *140*, 257–267. https://doi.org/10.1016/j.cell.2009.12.031.

79. Zhou, C., Slaughter, B.D., Unruh, J.R., Eldakak, A., Rubinstein, B., and Li, R. (2011). Motility and segregation of Hsp104-associated protein aggregates in budding yeast. Cell *147*, 1186–1196. https://doi.org/10.1016/j.cell.2011.11.002.

80. San Gil, R., Cox, D., McAlary, L., Berg, T., Walker, A.K., Yerbury, J.J., Ooi, L., and Ecroyd, H. (2020). Neurodegenerative disease-associated protein aggregates are poor inducers of the heat shock response in neuronal cells. J. Cell Sci. *133*, e60579. https://doi.org/10.1242/jcs.243709.

81. Klaips, C.L., Gropp, M.H.M., Hipp, M.S., and Hartl, F.U. (2020). Sis1 potentiates the stress response to protein aggregation and elevated temperature. Nat. Commun. *11*, 6271. https://doi.org/10.1038/s41467-020-20000-x.

82. Gomez-Pastor, R., Burchfiel, E.T., Neef, D.W., Jaeger, A.M., Cabiscol, E., McKinstry, S.U., Doss, A., Aballay, A., Lo, D.C., Akimov, S.S., et al. (2017). Abnormal degradation of the neuronal stress-protective transcription factor HSF1 in Huntington's disease. Nat. Commun. *8*, 14405. https://doi.org/10.1038/ncomms14405.

83. Chen, H.J., Mitchell, J.C., Novoselov, S., Miller, J., Nishimura, A.L., Scotter, E.L., Vance, C.A., Cheetham, M.E., and Shaw, C.E. (2016). The heat shock response plays an important role in TDP-43 clearance: evidence for dysfunction in amyotrophic lateral sclerosis. Brain *139*, 1417–1432. https://doi.org/10.1093/brain/aww028.

84. Iadanza, M.G., Jackson, M.P., Hewitt, E.W., Ranson, N.A., and Radford, S.E. (2018). A new era for understanding amyloid structures and disease. Nat. Rev. Mol. Cell Biol. *19*, 755–773. https://doi.org/10.1038/s41580-018-0060-8.

85. Sawaya, M.R., Hughes, M.P., Rodriguez, J.A., Riek, R., and Eisenberg, D.S. (2021). The expanding amyloid family: Structure, stability, function, and pathogenesis. Cell *184*, 4857–4873. https://doi.org/10.1016/j.cell.2021.08.013.

86. Fitzpatrick, A.W., and Saibil, H.R. (2019). Cryo-EM of amyloid fibrils and cellular aggregates. Curr. Opin. Struct. Biol. *58*, 34–42. https://doi.org/10.1016/j.sbi.2019.05.003.

87. Dobson, C.M., Knowles, T.P.J., and Vendruscolo, M. (2020). The Amyloid Phenomenon and Its Significance in Biology and Medicine. Cold Spring Harb. Perspect. Biol. *12*, a033878. https://doi.org/10.1101/cshperspect.a033878.

88. Jarrett, J.T., and Lansbury, P.T., Jr. (1993). Seeding "one-dimensional crystallization" of amyloid: a pathogenic mechanism in Alzheimer's disease and scrapie? Cell *73*, 1055–1058. https://doi.org/10.1016/0092-8674(93)90635-4.

89. Wright, C.F., Teichmann, S.A., Clarke, J., and Dobson, C.M. (2005). The importance of sequence diversity in the aggregation and evolution of proteins. Nature *438*, 878–881. https://doi.org/10.1038/nature04195.

90. Fändrich, M., and Dobson, C.M. (2002). The behaviour of polyamino acids reveals an inverse side chain effect in amyloid structure formation. EMBO J. *21*, 5682–5690. https://doi.org/10.1093/emboj/cdf573.

91. Krobitsch, S., and Lindquist, S. (2000). Aggregation of huntingtin in yeast varies with the length of the polyglutamine expansion and the expression of chaperone proteins. Proc. Natl. Acad. Sci. USA *97*, 1589–1594. https://doi.org/10.1073/pnas.97.4.1589.

92. Duennwald, M.L., Jagadish, S., Muchowski, P.J., and Lindquist, S. (2006). Flanking sequences profoundly alter polyglutamine toxicity in yeast. Proc. Natl. Acad. Sci. USA *103*, 11045–11050. https://doi.org/10.1073/pnas.0604547103.

93. Schindelin, J., Arganda-Carreras, I., Frise, E., Kaynig, V., Longair, M., Pietzsch, T., Preibisch, S., Rueden, C., Saalfeld, S., Schmid, B., et al. (2012). Fiji: an open-source platform for biological-image analysis. Nat. Methods *9*, 676–682. https://doi.org/10.1038/nmeth.2019.

94. Gietz, R.D., and Schiestl, R.H. (2007). High-efficiency yeast transformation using the LiAc/SS carrier DNA/PEG method. Nat. Protoc. *2*, 31–34. https://doi.org/10.1038/nprot.2007.13.

95. Scior, A., Preissler, S., Koch, M., and Deuerling, E. (2011). Directed PCR-free engineering of highly repetitive DNA sequences. BMC Biotechnol. *11*, 87. https://doi.org/10.1186/1472-6750-11-87.

96. Wach, A., Brachat, A., Alberti-Segui, C., Rebischung, C., and Philippsen, P. (1997). Heterologous HIS3 marker and GFP reporter modules for PCR-targeting in Saccharomyces cerevisiae. Yeast *13*, 1065–1075. https://doi.org/10.1002/(SICI)1097-0061(19970915)13:11<1065::AID-YEA159>3.0.CO;2-K.

97. Janssen, B.D., Diner, E.J., and Hayes, C.S. (2012). Analysis of aminoacyl- and peptidyl-tRNAs by gel electrophoresis. Methods Mol. Biol. *905*, 291–309. https://doi.org/10.1007/978-1-61779-949-5_19.

98. Pemberton, L.F. (2014). Preparation of yeast cells for live-cell imaging and indirect immunofluorescence. Methods Mol. Biol. *1205*, 79–90. https://doi.org/10.1007/978-1-4939-1363-3_6.

STAR★METHODS

KEY RESOURCES TABLE

REAGENT or RESOURCE	SOURCE	IDENTIFIER
Antibodies		
Mouse monoclonal anti-GFP	Roche	Cat#11814460001; RRID:AB_390913
Rabbit polyclonal anti-TagRFP (used to probe BFP)	Invitrogen	Cat#R10367; RRID:AB_2315269
Mouse polyclonal anti-Rqc2	This paper, custom synthesis performed by Singapore Advanced Biologics Pte. Ltd.	NA
Mouse monoclonal anti-FLAG	Sigma-Aldrich	Cat#F1804; RRID:AB_262044
Mouse monoclonal anti-HA	Roche	Cat#11583816001; RRID:AB_514505
Mouse monoclonal anti-ribosomal protein L3 (*S. cerevisiae*)	DSHB	Cat#ScRPL3; RRID:AB_1553774
Mouse monoclonal anti-Pgk1	Thermo Fisher Scientific	Cat#459250; RRID:AB_2532235
Mouse monoclonal anti-B-actin	Cell Signaling Technologies	Cat#3700; RRID:AB_2242334
Rabbit polyclonal anti-Yeast Sis1 (DnaJ)	Cosmo Bio Japan	Cat#COP-080051; RRID:AB_10709957
Goat polyclonal secondary anti-rabbit IgG, HRP-linked	Cell Signaling Technologies	Cat#7074; RRID:AB_2099233
Goat polyclonal secondary anti-mouse IgG, HRP-linked	Cell Signaling Technologies	Cat#7076; RRID:AB_330924
Goat anti-mouse IgG (H+L) Superclonal™ recombinant secondary antibody, AlexaFluor™ 647	Invitrogen	Cat#A28181; RRID:AB_2536165
Bacterial and virus strains		
TOP10 *E. coli* competent cells	Thermo Fisher Scientific	Cat#C404003
Stbl3™ *E. coli* competent cells	Thermo Fisher Scientific	Cat#C737303
Chemicals, peptides, and recombinant proteins		
37% w/v formaldehyde	Sigma	Cat#F8775
AlkPhos Direct Labelling module	cytiva	Cat#RPN3680
AscI	NEB	Cat#R0558
Bacto™ Yeast Extract	Gibco	Cat#212750
BamHI-HF	NEB	Cat#R3136
Benzonase	Sigma	Cat#E8263
CDP-*Star*	Sigma	Cat#C0712
ClaI	NEB	Cat#R0197
Cycloheximide	Sigma	Cat#1810
DAPI	Sigma	Cat# D9542
DMEM	Gibco	Cat#11960044
Doxycycline	Sigma	Cat#D9891
EcoRI-HF	NEB	Cat#R3101
FBS	Hyclone	Cat#SV30160.03
GlutaMax	Gibco	Cat#3505061
HindIII-HF	NEB	Cat#R3104
Hoechst 33342	Sigma	Cat#B2261
Lipofectamine 3000	Invitrogen	Cat#L3000015
MES	Sigma	Cat#M3671
MG132	Sigma	Cat#M7449
NucRed™ Live 647 ReadyProbes™	Invitrogen	Cat#R37106

(*Continued on next page*)

Continued

REAGENT or RESOURCE	SOURCE	IDENTIFIER
Penicillin-Streptomycin	Gibco	Cat#15140122
Peptone-A	Bio Basic	Cat#G213
Pierce Protease Inhibitor	Thermo Scientific	Cat#A32965
RIPA buffer	Sigma	Cat#R0278
SacI-HF	NEB	Cat#R3156
SuperSignal™ West Atto Ultimate Sensitivity Substrate	Thermo Scientific	Cat#A38554
SuperSignal™ West Pico PLUS Chemiluminescent Substrate	Thermo Scientific	Cat#34580
TRIzol™ reagent	Invitrogen	Cat#15596018
TURBO™ DNase	Invitrogen	Cat#AM2238
XbaI	NEB	Cat#R0145
XhoI	NEB	Cat#R0146
Yeast nitrogen base without amino acids	Sigma	Cat#Y0626
Zymolyase 100T	Nacalai Tesque Japan	Cat#07665-55
Critical commercial assays		
Bio-Rad Protein Assay Dye Reagent Concentrate	Bio-Rad, USA	Cat#5000006
Pierce™ 660nm Protein Assay Reagent	Thermo Scientific	Cat#22660
Ionic Detergent Compatibility Reagent for Pierce™ 660nm Protein Assay Reagent	Thermo Scientific	Cat#22663
GFP-Trap® magnetic agarose beads	ChromoTek	Cat#gtma
Deposited data		
Original data for western blots, microscopy images, and amino acid analyses	This paper	Mendeley Data: https://doi.org/10.17632/vfj9sf7s8t.1
Experimental models: Cell lines		
Human: HEK293T	ATCC	Cat#CRL-3216™ ; RRID:CVCL_0063
Human: HeLa	ATCC	Cat#CCL-2™; RRID:CVCL_0030
Human: SH-SY5Y	ATCC	Cat#CRL-2266™; RRID:CVCL_0019
Experimental models: Organisms/strains		
S. cerevisiae: BY4741	Euroscarf	N/A
All yeast strains derived from BY4741 are listed in Table S1	NA	N/A
S. cerevisiae: R1158 (Yeast Tet-promoters Hughes yTHC parental strain)	Horizon Discovery	Cat#YSC1210
Oligonucleotides		
Northern blot probe to detect tA^{IGC}: TGGACGAGTCCGGAATCGAACCGG AGACCTCTCCCATGCTAAGGGAGC GCGCTACCGACTACGCCACACGCCC	This paper	NP_tA(AGC)F
Northern blot probe to detect tA^{UGC}: TGGACGCAACCGGAATCGAACCGA TGACCTCTTCCTTGCAAGGGAAGC GCGCTACCAACTGCGCCATGTGCCC	This paper	NP_tA(UGC)G
Northern blot probe to detect tT^{AGU}: TGCTTCCAATCGGATTTGAACCGAT GATCTCCACATTACTAGTGTGGCG CCTTACCAACTTGGCCATAGAAGC	This paper	NP_tT(AGU)N2

(*Continued on next page*)

Continued

REAGENT or RESOURCE	SOURCE	IDENTIFIER
Northern blot probe to detect tT^{CGU}: TGCCCTCTGTGGGAATTGAACCCA CGATCCCCGCATTACGAGTGCGAT GCCTTACCACTTGGCCAAAAGGGC	This paper	NP_tT(CGU)K
Northern blot probe to detect tT^{UGU}: TGCCACCTGTCAGAATTGAACTAA CGACCTTTGCATTACAAGTGCAAC GCTCTACCACTAAGCTAAGGAGGC	This paper	NP_tT(UGU)G2
Northern blot probe to detect tR^{ICG} (control): CTTCCCCGCCAGGACTTGAACCTGGAAT CTTCTGGTTCGTAGCCAGACGCCGTGAC CATTGGGCCACGAGGAA	This paper	NP_tR(ACG)D
Primer: CATGGATCCTCATGTAGTTGTGGTT GTAGTCGTGGTTGTAGTTTTGTATA GTTCATCCAT	This paper	R_GFP-**T10**stop_BamHI:
Primer: CATGGATCCTCATGCAGCCGCAGC TGCGGCTGCAGCTGCAGCTTTGTA TAGTTCATCCAT	This paper	R_GFP-**A10**stop_BamHI:
Primer: AGCAAGCTTTCACGTAGTTGTAGTT GTGGTCGTAGTTGTAGTTGTAGTCG TGGTTGTAGTCGTGGTTGTAGTGGA TCCCTTGTACAGCTC	This paper	R_GFP-**T20**stop_BamHI
Primer: AGCAAGCTTTCAGGCTGCAGCCGCA GCTGCGGCTGCAGCTGCGGCAGCCG CAGCTGCGGCTGCAGCTGCAGCGGA TCCCTTGTACAGCTC	This paper	R_GFP-**A20**stop_BamHI
Recombinant DNA		
p416 25Q GAL	Krobitsch et al.[91]	RRID:Addgene_1185
p416 103Q GAL	Krobitsch et al.[91]	RRID:Addgene_1186
GAL 46Q+ProGFPp416	Duennwald et al.[92]	RRID:Addgene_15581
GAL 72Q+ProGFPp416	Duennwald et al.[92]	RRID:Addgene_15582
The full lists of plasmids used in this paper are listed in Tables S2 (Yeast) and S4 (Mammalian)	This paper	N/A
Software and algorithms		
BioRender	BioRender	www.biorender.com; RRID:SCR_018361
FIJI	Schindelin et al.[93]	https://imagej.net/software/fiji/; RRID:SCR_002285
FlowJo	BD Biosciences	RRID:SCR_008520
GraphPad Prism version 10.0.3	GraphPad Software, Boston, Massachusetts USA	www.graphpad.com; RRID:SCR_002798
ZEN Blue 3.4	Carl Zeiss, Germany	RRID:SCR_013672
R statistical software version 4.4.1	R Project	https://www.r-project.org; RRID:SCR_002394
Other		
Amersham Hybond-N+	Cytiva	Cat#RPN303B
ChemiDoc MP Imaging System	Bio-Rad	Cat#12003154
Amersham ImageQuant 800 Fluor	Cytiva	Cat#29399484
LSM980 with Airyscan2 confocal microscope	Zeiss	NA
Mini Trans-Blot© cell	Bio-Rad	Cat#1703930
Nitrocellulose membrane, 0.45 um	Bio-Rad	Cat#1620115

(*Continued on next page*)

Continued

REAGENT or RESOURCE	SOURCE	IDENTIFIER
Precellys Evolution Homogeniser with Cryolys Evolution Cooling Unit	Bertin Instruments	Cat#P000062-PEVO0-A and #P000671-CLYS2-A
TE70X Semi-Dry Transfer unit	Hoefer	Cat#TE70X

EXPERIMENTAL MODEL AND STUDY PARTICIPANT DETAILS

Yeast strains

S. cerevisiae strain BY4741 (MATa his3Δ1 leu2Δ0 met15Δ0 ura3Δ0) was obtained from Euroscarf. All other strains reported in this paper were derived from BY4741 and are listed in Table S1. Yeast cells were cultured at 30°C unless otherwise stated in either YPD (1% yeast extract, 2% peptone, 2% glucose) or synthetic drop-out media, consisting of 0.67% yeast nitrogen base supplemented with an appropriate carbon source (2% of glucose, raffinose or galactose) and amino acids. Details of yeast culture are described under method details.

Human cell lines

HEK293T (embryonic), HeLa (female) and SH-SY5Y (female) cells were obtained from ATCC. The cells were maintained in Dulbecco's Modified Eagle Medium (DMEM) supplemented with 10% (v/v) fetal bovine serum (FBS), GlutaMax, penicillin and streptomycin at 37°C in a humidified atmosphere containing 5% CO_2. Details of cell culture are described under method details.

METHOD DETAILS

Yeast culture and transformation

Yeast were cultured at 30°C unless otherwise stated in either YPD (YPD: Yeast extract-Peptone-Dextrose medium; 1% Bacto-yeast extract, 2% Bacto-peptone, 2% glucose) or synthetic drop-out (SD) media, consisting of 0.67% yeast nitrogen base without amino acids (Sigma, Y0626) supplemented with an appropriate carbon source of 2% glucose (Sigma, G8270), raffinose (Nacalai Tesque Japan, 30001-15) or galactose (Sigma, G0625) and amino acids: 0.04 g/L adenine sulfate (Sigma, A8626), 0.04 g/L L-tryptophan (Sigma, T0254), 0.02 g/L L-arginine hydrochloride (Sigma, A5006), 0.03 g/L L-tyrosine (Sigma, T3754), 0.03 g/L L-lysine hydrochloride (Sigma, L5626), 0.05 g/L L-phenylalanine (Sigma, P2126), 0.1 g/L L-glutamic acid (Sigma, G1626), 0.1 g/L L-asparagine (Sigma, A8381), 0.15 g/L L-valine (Sigma, V0500), 0.2 g/L L-threonine (Sigma, T8625), 0.375 g/L L-serine (Sigma, S4500), 0.02 g/L L-methionine (Sigma, M9625), 0.02 g/L uracil (Sigma, U0750), 0.02 g/L L-histidine hydrochloride (Sigma, 53370), 0.06 g/L leucine (Sigma, L8000). Where indicated, cycloheximide (1 ng/mL, Sigma, 1810) or doxycycline (10 μg/mL, Sigma, D9891) were supplemented.

BY4741 has the [*PIN*$^+$] phenotype. To generate the [*pin*$^-$] strain, WT [*PIN*$^+$] was plated on YPD containing 3 mM guanidine hydrochloride (Sigma, G3272).[58] To confirm the loss of [*PIN*$^+$], GFP-tagged Rnq1 (Rnq1-GFP) was expressed. Endogenous Rnq1 prions in [*PIN*$^+$] cells template Rnq1-GFP aggregation, resulting in puncta formation (Figure S5F). In contrast, Rnq1-GFP remains diffuse in [*pin*$^-$] cells.

Yeast plasmid transformations were performed using the LiAc/SS carrier DNA/PEG method.[94] Briefly, yeast cells in logarithmic phase were centrifuged and washed twice with water before heat shock at 42°C for 20 min with a mixture of lithium acetate (LiAc; Sigma, 62393), single-stranded carrier DNA (SS carrier; Sigma, D1626), polyethylene glycol (PEG 3350; Sigma, P4338) and exogenous DNA. Transformed cells were plated on appropriate selection media. Yeast integrating plasmids were linearised with an appropriate restriction enzyme before transformation, and correct genomic integration was confirmed via PCR using primers complementary to upstream, downstream, and within the insert.

Plasmid design

All plasmids used are listed in Table S2 (yeast) and Table S4 (mammalian).

Plasmids were constructed using standard cloning procedures using appropriate primers and restriction enzymes and were verified using Sanger sequencing (Bio Basic Asia Pacific).

The stalling reporter CGA_4 was synthesised by inserting four CGA repeats directly after GFP using a primer. This fragment was cloned into the yeast vector pRS416GAL1 under the *GAL1* promoter using the restriction sites XbaI and BamHI, followed by 2x HA tags flanked by BamHI and HindIII and mCherry flanked by HindIII and ClaI.

For tRNA overexpression plasmids, we amplified the respective tRNA coding region together with 5' and 3' flanking sequences (more than 150 bp each), which contain the native promoter and terminator of the gene. Amplicons were inserted using SacI and BamHI into pRS425 plasmids (2μ, multi-copy).

We designed C-terminal polyamino acid tail constructs to incorporate a mixture of codons for each amino acid, with proportions determined according to the codon usage in *S. cerevisiae*. Tails were created either with primers or with synthesized gene fragments

(Twist Bioscience, USA). Primers were used to extend GFP with T10, A10, T20 and A20. T20 and A20 sequences were flanked by BamHI and HindIII. There were four main gene fragment designs. First, T30 and S30 were synthesized in the form: BamHI-T/S30-stop codon (TGA)-HindIII. Second, Q30 and N30 were initially synthesized as shorter fragments of Q16 and N16 and were subsequently extended to 30 amino acid repeats using a PCR-free method.[95] Cloning using Type IIS restriction sites allowed for scarless extension of the polyamino acid sequence to 30 repeats. Third, the rest of the tails were synthesized in the form BamHI-Tail-stop codon (TGA)-EcoRI-spacer-HindIII. Tails were cloned into yeast vectors under the *GAL1* promoter, or in the mammalian vector pcDNA3.1(-) under the CMV promoter, downstream of XbaI-GFP/BFP-BamHI. The list of artificial CAT tails can be found in Table S3. Fourth, N-terminal FLAG- and HA-tagged polythreonine tails (FLAG/HA-T30/T20/T10) were synthesized in the form: XbaI-FLAG/HA-Tail-stop codon (TGA)-EcoRI-spacer-HindIII and cloned into the yeast vector pRS416 under the *GAL1* promoter. All DNA constructs in this study, including polyamino acid tails, were verified using Sanger sequencing.

To synthesize fluorescent-tagged organelle markers for the nucleus (Nic96-GFP or mCherry) and the yeast vacuole (Vph1-mCherry), *NIC96* and *VPH1*, together with their promoters, were inserted into pRS41X yeast vectors using the restriction sites SacI-BamHI and SacI-HindIII respectively. For Nic96 reporters, either mCherry (BamHI-XhoI) or GFP (BamHI-ClaI) were inserted immediately downstream of *NIC96*. For Vph1 reporters, mCherry (HindIII-XhoI) was inserted.

The HSR reporter strains were generated by integrating the HSR plasmid, containing the pRS403 backbone, into WT, *ltn1*Δ or *ltn1*Δ/*RQC2* overexpression cells via homologous recombination within the *HIS3* locus. The HSR plasmid design was adapted from a previous report.[33] A GFP reporter was cloned under a crippled *CYC1* promoter that lacks activity, with regulation occurring exclusively through four tandem repeats of the heat shock element (HSE) upstream. Consequently, GFP expression levels are proportional to the activity of heat shock factor 1 (Hsf1). mCherry, cloned under the constitutive *TEF2* promoter, served as an internal control, indicating overall cellular gene expression level. mCherry-tagged chaperone strains (Sis1-mCh, Ydj1-mCh, Ssa1-mCh, Ssa2-mCh and Hsp104-mCh) were generated through homologous recombination using PCR amplicons comprising: mCherry-ADH1 terminator and a *HIS3* marker expression cassette, flanked by 45 bp homologous sequences allowing for homologous recombination at the C terminus of the target chaperone gene. Amplicons were amplified using the plasmid pFA6a-mCherry-tADH1-pTEF1-skHIS3-tTEF1. GFP in the original plasmid[96] was replaced by mCherry in this study using HindIII and AscI.

Vectors for C-terminal GFP-tagged Huntingtin proteins of various polyglutamine lengths (Htt25Q, Htt46Q, Htt72Q and Htt103Q) were obtained from Addgene (#1185, #15581, #15582 and #1186, respectively) and used directly without modification in yeast. Htt25Q, Htt46Q and Htt72Q, along with the GFP tag, were PCR amplified from their yeast vector and inserted into pcDNA3.1(-) using the restriction sites XbaI and XhoI.

Mammalian cell culture and transfection

HEK293T, HeLa and SH-SY5Y cells were obtained from ATCC. Cell lines were cultured in DMEM (Gibco, 11960044) supplemented with 10% FBS (GE HyClone, SV30160.03), 1X GlutaMax (Gibco, 3505061), 100 U/ml penicillin and 100 μg/ml streptomycin (Gibco, 15140122) at 37°C in a humidified atmosphere containing 5% CO_2.

Plasmid transfection was performed using Lipofectamine 3000 (Invitrogen, L3000015) into 70% confluent cell culture.

Yeast lysate preparation

Cells were cultured overnight in appropriate selective media and harvested at OD_{600} = 0.4-1 to obtain minimally OD_{600} = 40 of cells. Cells were harvested by centrifugation at 10,000 x g for 7 min at 4°C (Beckman High-Speed Centrifuge J-25 with JA-14 rotor, Beckman Coulter). Cell pellets were washed twice with water, flash frozen with liquid nitrogen and either stored at -80°C for future use or immediately lysed via glass bead homogenization (Precellys Evolution Homogenizer, Bertin Instruments, France). Around 500 μL of glass beads (425-600 μm, Sigma, G8772) and lysis buffer (25 mM Tris-Cl pH 7.4, 150 mM NaCl, 1 mM EDTA, 5% glycerol) supplemented with 1X Pierce protease inhibitor (Thermo Scientific, A32965) were added to each cell pellet. Pellets were homogenized at 8,000 rpm at 0°C for 4 cycles of 40s with 90s rest between each cycle. Cell debris was cleared by 2 rounds of low-speed centrifugation at 2,000 x g for 5 min at 4°C. Protein concentrations were determined using the Bradford assay (Bradford's reagent, Bio-Rad, 5000006).

Immunoprecipitation

Immunoprecipitation for Figure S1D was performed with 500 μg of clarified lysate according to the manufacturer's protocol. Briefly, lysates were incubated with 12.5 μL of GFP-Trap® magnetic agarose beads (ChromoTek) for 1 hour at 4°C, washed 3 times in wash buffer (10 mM Tris/Cl pH 7.5, 150 mM NaCl, 0.05 % Nonidet™ P40 Substitute, 0.5 mM EDTA), eluted in protein solubilization buffer and boiled for 5 min before loading.

Mammalian cell lysate preparation

Cell harvesting was performed 1-2 days post-transfection. Cells were harvested using centrifugation and cell pellets were flash frozen using liquid nitrogen and kept at -80°C for future use.

For SDS-PAGE, cells were disrupted in RIPA buffer (Sigma, R0278) containing Benzonase (Sigma, E8263) and Pierce protease inhibitor (Thermo Scientific, A32965) on ice for 5 min. Crude lysates were centrifuged at 2,000 x g for 5 min at 4°C and their

concentrations were measured using Pierce 660 nm protein assay reagent (Thermo Scientific, 22660) containing ionic detergent compatibility reagent (Thermo Scientific, 22663).

For SDD-AGE, the harvested cells were sonicated by Bioruptor™ Pico (Diagenode; 30 sec of on and 30 sec of off with 10 cycles) in lysis buffer (25 mM Tris-Cl pH 7.4, 150 mM NaCl, 1 mM EDTA, 5% glycerol) with protease inhibitor. Crude lysate was centrifuged at 2,000 x g for 5 min at 4°C and protein concentrations were determined by Bradford assay.

Immunoblotting

For SDS-PAGE, lysates were boiled with protein solubilization buffer (2% SDS, 5% β-mercaptoethanol, 10% glycerol, 0.25 M Tris-Cl pH 7.4, 0.005% bromophenol blue) at 98°C for 5 min. Samples were resolved using either 4-12% gradient or 4% stacking and 12% resolving Bis-Tris gels in MES buffer (0.05 M MES, 0.05 M Tris, 1 mM EDTA, 0.1% SDS, 5 mM sodium bisulfite). Electro-transfer was performed at 350 mA for 1 h using the Mini Trans-Blot© cell (Bio-Rad) in Towbin buffer (25 mM Tris, 192 mM glycine, 0.5% SDS, 20% methanol).

To resolve high molecular weight aggregates, samples prepared by cell homogenization were resolved with semi-denaturing detergent agarose gel electrophoresis (SDD-AGE) as previously described[38] with minor modifications. Lysate samples were incubated with SDD-AGE sample buffer (20 mM Tris-acetate, 0.5 mM EDTA, 5% glycerol, 2% SDS, 0.005% bromophenol blue) at 25°C for 10 min and run on a 1.5% agarose gel made with TAE buffer (40 mM Tris-acetate, 1 mM EDTA) containing 0.1% SDS at 4°C at 75 V for 3 h. Downward capillary transfer of proteins was performed overnight at room temperature using SDD transfer buffer (10 mM Tris-Cl).

Blots were blocked in 3% milk (Sigma, 70166) for at least 30 min before overnight incubation with the appropriate primary antibody at 4°C. Blots were incubated for 1h at room temperature with secondary antibodies (1:3000, anti-mouse IgG, HRP-linked #7076 or anti-rabbit IgG, HRP-linked #7074, Cell Signaling Technology).

Immunodetection was performed with SuperSignal™ West Pico PLUS Chemiluminescent Substrate (Thermo Scientific, 34580) or SuperSignal™ West Atto Ultimate Sensitivity Substrate (Thermo Scientific, A38554) using the ChemiDoc MP Imaging System (Bio-Rad) or Amersham ImageQuant 800 (Cytiva). Images were processed using ImageJ software.

Northern blot for yeast tRNA

OD_{600} = 40 of log phase yeast cells were harvested by centrifugation and cell pellets were frozen using liquid nitrogen. Frozen cells were homogenized in TRIzol™ reagent (Invitrogen, 15596018) using the Precellys Evolution Homogeniser (Bertin Instruments, France). RNA was extracted via phenol/chloroform extraction and total RNA was treated with TURBO™ DNase (Invitrogen, AM2238) at 37°C for 30 min.

5 μg of purified total RNA was separated in 10% TBE-Urea polyacrylamide gel after deacylation using copper sulfate.[97] Gel was blotted on Amersham Hybond-N+ (Cytiva, RPN303B) using TE70X Semi-Dry Transfer unit (Hoefer, TE70X). Synthesized DNA probes for tRNA were labeled by Amersham AlkPhos Direct Labelling module (RPN3680). Labeled DNA probes were hybridized in AlkPhos Direct hybridization buffer at 55°C overnight. CDP-*Star* (Sigma, C0712) was used for signal generation. Fold changes of northern blot signals were determined using Image Lab Software (Bio-Rad).

Amino acid analysis

The CGA_{12} stalling reporter (GFP-CGA_{12}-mCherry) was induced overnight for the expression under the *GAL1* promoter with respective tRNA overexpression. Stalled GFP reporter proteins were isolated by immunoprecipitation as described above. 8 mg of clarified lysate in lysis buffer containing protease inhibitor was incubated with 25 μL of GFP-Trap® magnetic agarose beads (ChromoTek) for 1 hour at 4°C. After three washes, the beads were eluted in 60 μL buffer adjusted to pH 2.0. Eluates were subjected to amino acid analysis at the UC Davis Genome Center as described previously.[22] Graphs report the means of three samples. To visualize small changes in the molar percentages of threonine and alanine, only amino acids with content levels similar to threonine and alanine are graphed in Figures S1E and S1K.

Fluorescence microscopy

Live cell fluorescence microscopy was performed on yeast using the Zeiss LSM980 with Airyscan confocal microscope, ZEN Blue 3.4 using the Plan-Apochromat oil objective lens (63x, numerical aperture (NA) = 1.40, Carl Zeiss, Germany). Yeast cells were harvested in the logarithmic phase (OD_{600} < 1) and concentrated by centrifugation at 2,000 x g before 4 μL was used for imaging. For yeast cell counts, 3-5 fields (depending on cell density) of 3 biological replicates were taken for each sample using an inverted fluorescence microscope (Nikon Ti-eclipse inverted fluorescence microscope, Plan Apo VC 100x/1.40 oil objective lens, NIS-Elements AR Imaging Software ver3.22.00, Nikon, Japan) and counted using ImageJ software. During counting, brightness and contrast were raised for all images to ensure smaller puncta that may be present were counted.

Live cell fluorescence microscopy was performed on mammalian cells one to two days post-transfection using the Zeiss LSM980 with Airyscan2 confocal microscope, ZEN Blue 3.4 equipped with Plan-Apochromat objective lens (20x, NA = 0.8, Carl Zeiss, Germany). Cells were seeded in μ-Slide 8 Well high coverslips (Ibidi, 80806). To stain nuclei, Hoechst 33342 (Sigma, B2261) or NucRed™ Live 647 ReadyProbes™ reagent (Invitrogen, R37106) were added directly into media and incubated for half an hour before imaging. For mammalian cell counts, 3 fields of 3 biological replicates were imaged as above and counted using ImageJ software.

All microscopy experiments in this study were conducted using live yeast and human cells, with the exception of Figure 2F. All images were processed using ZEN Blue 3.4 and ImageJ software.

Live-cell FRAP

The FRAP (fluorescence recovery after photobleaching) assay was performed using the Zeiss LSM980 with Airyscan2 equipped with a 1.4 numerical aperture (NA) Plan-Apochromat 63x oil-immersion lens (Carl Zeiss, Germany). The region of interest was bleached using a 488 nm laser at 100% laser power with 10 iterations. Time-lapse images were captured for 2 minutes using the attenuated laser power intensity (0.05%). For each indicated time point, the fluorescence intensity of the bleached region was normalized to the fluorescence intensity measured on another cell within the same imaging field. The normalized fluorescence intensity of pre-bleaching was set to 100% and the point of bleaching was set to 0%. Data were analyzed and quantified using ImageJ software and plotted using GraphPad Prism.

Yeast immunofluorescence microscopy

Yeast immunofluorescence microscopy was performed using a protocol adapted from a previous report.[98] Plasmid expression was induced by culturing in selective media with galactose at 30°C followed by fixation with 1/10th volume of 37% w/v formaldehyde (Sigma, F8775) before the growth exceeded OD_{600} = 1. The cell wall was digested using 1 mg/ml zymolyase 100T (Nacalai Tesque Japan, 07665-55) in 100 mM sodium phosphate buffer (pH 6.5) containing 1.2 M sorbitol for 30 min at 30°C to form spheroplasts. Blocking was performed using PBS containing 2% BSA and 0.1% Tween-20 for 5 min at room temperature in a humidity chamber. This was followed by overnight incubation at 4°C with anti-Flag antibody (1:500 dilution, Sigma, F1804) in PBS containing 2% BSA and 0.1% Tween-20. On the next day, cells were treated with anti-mouse Alexa 647nm (1:1000, Invitrogen, A28181) as the secondary antibody.

Images were taken using the Zeiss LSM980 with Airyscan2 confocal microscope, ZEN Blue 3.4 equipped with Plan-Apochromat objective lens (63x, NA = 1.40, Carl Zeiss, Germany).

Spotting growth assay

Cells refreshed in SD raffinose media were diluted to a starting OD_{600} of 0.1 before 5-fold serial dilutions were performed. 4 μL of each dilution was spotted onto SD glucose (control/uninduced) and galactose (induced) plates. Where indicated, cycloheximide or doxycycline was supplemented to a final concentration of 1 ng/mL or 20 μg/mL respectively. Plates were incubated at 30°C for 48-72 h and imaged (ChemiDoc MP Imaging System, Bio-Rad). Images were processed using ImageJ software.

Flow cytometry

All cells were maintained at 25°C. Approximately OD_{600} = 1 of logarithmic phase cells were pelleted, washed once with 1X PBS, and resuspended in 1 mL of 1X PBS. Fluorescence measurements were performed at room temperature using the BD LSRFortessa™ X-20 Cell Analyzer with the BD FACSDiva™ software (BD Biosciences). FlowJo™ v10 software (BD Biosciences) was used for analyses and GraphPad Prism (version 10.0.3, GraphPad Software) was used to generate graphs.

Median fluorescence values were used for calculations. Graphs report $\log_2$ GFP/mCh fluorescence ratios normalized to the appropriate controls.

QUANTIFICATION AND STATISTICAL ANALYSIS

Statistical analyses performed are indicated in the figure legends of the relevant data, including n values. In all cases, analyses were performed using Microsoft Excel, R Statistical Software (version 4.4.1) and/or GraphPad Prism (version 10.0.3). Error bars represent standard error of the mean. Statistical significance was assessed using Student's t test (two-tailed, unpaired) for experiments with two sample groups and one-way ANOVA analysis followed by Tukey's range test for experiments with more than two sample groups. All *p* values are reported to three significant figures.